1D-velocity structure and seismotectonics of the Ecuadorian margin inferred from the 2016 Mw7.8 Pedernales aftershock sequence

Sergio Leon-Rios*, *Geophysical Institute, Karlsruhe Institute of Technology, 76187 Karlsruhe, Germany*

Hans Agurto-Detzel, Geoazur; Université Côte d'Azur, IRD, CNRS, Observatoire de la Côte d'Azur, Géoazur, Valbonne, France

Andreas Rietbrock, *Geophysical Institute, Karlsruhe Institute of Technology, 76187 Karlsruhe, Germany; School of Environmental Sciences, University of Liverpool, Liverpool L69 3GP, UK*

Alexandra Alvarado, *Instituto Geofísico - Escuela Politécnica Nacional, Ladrón de Guevara E11-253 Andalucía, Quito 170525, Ecuador*

Susan Beck, *Department of Geosciences, University of Arizona, 1040 East 4th Street, Tucson, AZ 85721, USA*

Phillipe Charvis, *Université Côte d'Azur, IRD, CNRS, Observatoire de la Côte d'Azur, Géoazur, Valbonne, France*

Benjamin Edwards, School of Environmental Sciences, University of Liverpool, Liverpool L69 3GP, UK

Yvonne Font, *Université Côte d'Azur, IRD, CNRS, Observatoire de la Côte d'Azur, Géoazur, Valbonne, France*

Tom Garth, *Department of Earth Sciences, University of Oxford, South Parks Road, Oxford, OX1 3AN, UK*

Mariah Hoskins, *Department of Earth and Environmental Sciences, 1 West Packer Avenue, Lehigh University, Bethlehem, Pennsylvania 18015, USA*

Colton Lynner, *Department of Geosciences, University of Arizona, 1040 East 4th Street, Tucson, AZ 85721, USA*

Anne Meltzer, *Department of Earth and Environmental Sciences, 1 West Packer Avenue, Lehigh University, Bethlehem, Pennsylvania 18015, USA*

Jean Matthieu Nocquet, *Université Côte d'Azur, IRD, CNRS, Observatoire de la Côte d'Azur, Géoazur, Valbonne, France. // Institut de Physique du Globe de Paris, Sorbonne Paris Cité, Université Paris Diderot, UMR 7154 CNRS, Paris, France.*

Marc Regnier, *Université Côte d'Azur, IRD, CNRS, Observatoire de la Côte d'Azur, Géoazur, Valbonne, France*

Frederique Rolandone, *Sorbonne Université, CNRS-INSU, ISTeP UMR 7193, Paris, France. // Université Côte d'Azur, IRD, CNRS, Observatoire de la Côte d'Azur, Géoazur, Valbonne, France*

Mario Ruiz, *Instituto Geofísico - Escuela Politécnica Nacional, Ladrón de Guevara E11-253 Andalucía, Quito 170525, Ecuador*

Lillian Soto-Cordero, *Department of Earth and Environmental Sciences, 1 West Packer Avenue, Lehigh University, Bethlehem, Pennsylvania 18015, USA*

* corresponding author:

Sergio Leon-Rios

Geophysical Institute, Karlsruhe Institute of Technology

Hertzstr. 16, Geb.6.42, 76187. Karlsruhe, Germany

sergio.leon-rios@kit.edu

ABSTRACT

On April 16th 2016 a Mw 7.8 earthquake ruptured the central coastal segment of the Ecuadorian subduction zone. Shortly after the earthquake, the Instituto Geofisico de la Escuela Politecnica Nacional of Ecuador, together with several international institutions deployed a dense, temporary seismic network to accurately categorize the post-seismic aftershock sequence. Instrumentation included short-period and broadband sensors, along with Ocean Bottom Seismometers. This deployment complemented the permanent Ecuadorian seismic network and recorded the developing aftershock sequence for a period of one year following the main-shock. A subset of 345 events with $M_L > 3.5$, were manually picked in the period of May to August 2016, providing highly accurate P- and S-onset times. From this catalogue, a high-quality dataset of 227 events, with an azimuthal gap < 200°, are simultaneously inverted for, obtaining the minimum 1D velocity model for the rupture region, along with hypocentral locations and station corrections. We observe an average Vp/Vs of 1.82 throughout the study region, with relatively higher Vp/Vs values of 1.95 and 2.18 observed for the shallowest layers down to 7.5 km. The high relative Vp/Vs ratio (1.93) of the deeper section, between 30 km and 40 km, is attributed to dehydration and serpentinization processes. For the relocated seismicity distribution, clusters of events align perpendicular to the trench, and crustal seismicity is also evidenced, along with earthquakes located close to the trench axis. We also compute Regional Moment Tensors to analyze the different sources of seismicity after the mainshock. Aside from thrust events related to the subduction process, normal and strike-slip mechanisms are detected. We suggest that the presence of subducting seamounts coming from the Carnegie Ridge act as erosional agents, helping to create a scenario which promotes locking and allows seismicity to extend up to the trench, along zones of weakness activated after large earthquakes.

KEYWORDS: 2016 Pedernales earthquake, Ecuador, velocity model, subduction zone, regional moment tensor, aftershock sequence.

1. INTRODUCTION

The South American subduction zone has a long history of large megathrust earthquakes and in the past decades a variety of different types of seismicity have been identified, including repeating earthquakes, seismic swarms and slow slip events. During the last century, the Ecuadorian-Colombian margin has experienced several major earthquakes (Ramirez, 1968; Kelleher, 1972; Abe, 1979; Herd et al., 1981; Kanamori and McNally, 1982; Mendoza and Dewey, 1984; Beck and Ruff, 1984; Swenson and Beck, 1996). More recently, slow slip events have been observed (Mothes et al., 2013; Vallee et al., 2013; Chlieh et al., 2014; Segovia et al., 2015; Vaca et al., 2018; Collot et al., 2017; Rolandone et al., 2018), in addition to seismic swarms (Segovia, 2001; Segovia, 2009; Vaca et al., 2009) and repeating earthquakes (Rolandone et al., 2018) (Figure 1).

In 1906 a megathrust earthquake Ms 8.7 (Kelleher, 1972), re-estimated to Mw 8.8 (Kanamori and McNally, 1982) and more recently to Mw 8.4 (Yoshimoto et al., 2017), ruptured the subduction segment along central and northern Ecuador and southern Colombia generating severe destruction which reached up to 100 km inland. The rupture extent of this earthquake is still under discussion. Whilst Kanamori and McNally (1982) suggested a rupture of approximately 500 km length, Yoshimoto et al., (2017) proposed a smaller rupture area mainly located near the trench. The 1906 earthquake also caused permanent coastal uplift and generated a destructive tsunami (Ramirez, 1968; Kelleher, 1972; Abe, 1979; Herd et al., 1981; Kanamori and McNally, 1982). Subsequently, smaller earthquakes of diverse magnitudes (between Mw 7.0 to Mw 8.2) ruptured with thrust mechanisms, leading to several authors proposing a segmentation of the subduction zone along the northern Ecuadorian margin (i.e. Marcaillou et al., 2006; Gailler et al., 2007). In 1942, a Mw 7.8 earthquake occurred close to the coastal city of Pedernales affecting an area of ~200 km x ~90 km. The epicenter was located at the southern edge of the rupture region, suggesting that the event propagated to the NE (Kelleher, 1972; Swenson and Beck, 1996). In 1958, the Mw 7.7 Colombia-Ecuador earthquake (Kanamori and McNally, 1982) broke a small segment of the 1906 megathrust earthquake in the offshore portion of the Esmeraldas province to the North. Like the 1942 earthquake, the 1958 event showed a rupture propagation in the NE direction (Rothe, 1969; Kelleher, 1972; Mendoza and Dewey, 1984). Finally, in 1979, the largest event of this series of major earthquakes occurred close to the

Ecuadorian-Colombian border with magnitude of Mw 8.2 also rupturing in a NE direction along ~230 km of the margin (Herd, 1981; Kanamori and Given, 1981: Beck and Ruff, 1984).

Between the equator and south of the Carnegie Ridge (CR), there have been few large subduction earthquakes recorded (Egred, 1968; Dorbath et al., 1990; Bilek et al., 2010) with only two events of Mw>7.0 (in 1956 and 1998) occurring close to Bahia Caraquez (ISC-GEM catalogue, Storchak et al., 2013). However, a high rate of seismicity up to Mw 6.5 has been registered in this region (Vallee et al., 2013) suggesting that the accumulated stresses are released by different mechanisms than in the northern segment (White et al., 2003; Agurto-Detzel et al., *2019*). Moreover, the area shows a complex slip behavior, with different types of seismic activity highlighted in Figure 1.

The Mw 7.8 Pedernales earthquake occurred in 2016 and led to the largest earthquake-related loss of life (668, Lanning et al., 2016) in Ecuador since the 1987, Mw 7.1 Salado-Reventador event, which occurred in the Andean volcanic arc that killed around 1000 people (Bolton et al., 1991; Beauval et al., 2010). The 2016 earthquake also affected the Ecuadorian economy due to widespread destruction of houses, hotels and hospitals (Lanning et al., 2016). One month after the earthquake, a dense temporary network (10-30 km station spacing) was deployed in collaboration with the Instituto Geofisico de la Escuela Politecnica Nacional (IGEPN) and several international institutions covering the rupture area. Instrumentation included Ocean Bottom Seismometers (OBS), inland short period and broadband sensors, which complemented the stations of the permanent Ecuadorian seismic network (Alvarado et al., 2018). The combined array recorded the unfolding aftershock sequence up to one year after the mainshock. Although large subduction thrust earthquakes are well documented historically, occurring extensively throughout the entire South American margin, it is only over the last decade that dense monitoring seismic networks have been deployed to record the aftershock sequences of such events. This allows for highly accurate hypocentral relocations enabling detailed investigations into the physical processes occurring within the rupture zone.

One of the major limitations in imaging the seismicity distribution along the Ecuadorian margin is the lack of a robust and well constrained velocity model for the area. The unprecedented seismic coverage provided by the international aftershock deployment offers a unique opportunity to better resolve the velocity structure of this region with the

Pedernales earthquake sequence. The recorded data will improve our knowledge of the seismotectonic structures, such as the CR and the Atacames seamounts, along with understanding the mechanisms that control subduction processes in the area.

Although the Ecuadorian margin has been widely studied, there is still no consensus on a representative one-dimensional (1D) velocity model. An improved 1D regional model together with well located aftershocks recorded by our dense seismic monitoring network will provide a better constrained seismic velocities in the area and, the foundation and starting model for future detailed 3D seismic imaging.

Currently, the available velocity models for the Ecuadorian margin are usually focused in small areas or have limited resolution due to the lack of instruments monitoring the offshore and coastal portion of the country; they are also affected by along strike heterogeneities observed in the region. At present, the national network of seismographs of the geophysical institute (RENSIG) from IGEPN uses a five-layer model (called ASW; for detailed values see Font et al. (2013)) and is used by the IGEPN for locating tectonic events in Ecuador. It, therefore, results in large errors in hypocenter location, especially regarding depth of subduction related seismicity (See Supplementary Material 1). Font et al. (2013) built an *a-priori* three-dimensional P-wave velocity model for the Ecuadorian subduction margin (4° N – 6° S, 83° W – 77° W), obtained via a joint compilation of marine seismics, gravimetric data, geological observations and seismicity of the region. The model is an improvement for the forearc and provides better hypocentral solutions for the coastal area but has limited capabilities due to the absence of an S-wave velocity model. Gailler et al. (2007) inverted wide-angle seismic data to describe deep structures present offshore of the Ecuadorian – Colombian border. In the same area, Agudelo et al. (2009) also improved the structural model using a combined data set of multichannel seismic reflection and wide-angle data. Garcia Cano et al. (2014) provide a 3D velocity model encompassing the rupture of the 1958 earthquake. Both models provide insights about offshore velocities. Further to the south of our study area, Calahorrano et al. (2008) developed a velocity model using marine seismic experiments representing the area close to the Gulf of Guayaquil. However, all three models are located outside of the Pedernales rupture area and outside the area covered by our temporary seismic array. Finally, Graindorge et al. (2004) analyzed the velocity structure in the Carnegie Ridge (CR) area using onshore and offshore wide-angle

data to calculate a two-dimensional model. Although our array covers a portion of the CR, this model is not appropriate for the whole area covered by the array due to the anomalous structure of this bathymetric feature.

Using high quality manually picked arrival times (P and S), we develop a minimum 1D velocity model for P- and S-wave velocities of the area affected by the Pedernales earthquake and post-seismic sequence. Based on a Monte Carlo-like approach in which we use a set of 5000 randomly perturbed velocity models as starting models for our inversion, we obtain a new robust minimum 1D velocity model for our study area. Finally, we analyze in detail the seismicity recorded offshore Bahia Caraquez, close to the trench, by determining Regional Moment Tensors (RMTs) to explore the correlation between the distribution of the events, the seismogenic contact and possible faults that might be re/activated due to the mainshock.

2. SEISMO-TECTONIC SETTING OF THE PEDERNALES EARTHQUAKE

2.1 Structural setting

The Ecuadorian margin is dominated by a convergent regime that involves the subducting oceanic Nazca plate and the overriding continental South American plate. This process occurs with a relative convergence rate of 55 mm/yr (Kendrick et al., 2003) in the N80°E direction. The margin is highly segmented and mainly of erosional type (Collot et al., 2002; Gailler et al., 2007; Marcaillou et al., 2016) creating diverse patterns in seismicity in the subducting and overriding plates as well as along the plate interface. Broadly, the Ecuadorian territory (1°N – 3°S) can be divided into three main domains extending inland from the margin (Jaillard et al., 2000) and our study area comprises mainly along domain (I) and part of domain (II). The profile A, in Figure 1b, shows the marine forearc including a small layer of sediments of 500 m to 1000 m thick. The coastal region is characterized by the presence of bathymetric features such as the aseismic CR. The CR (~280 km wide and 2 km high) is located near the Ecuadorian trench between latitude 0° and 2°S (see Figure 1a). The CR was formed by the Galapagos hot-spot located about 1000 km west of the coastline of Ecuador and is currently subducting in an ENE direction. The marine forearc has a series of seamounts such as the Atacames chain which subduct beneath the South American plate and is inferred to play an important role in the nucleation of large subduction earthquakes (Marcaillou et al., 2016). The coastal region shows accreted oceanic terranes from the late

Cretaceous-Paleogene period. The width of this domain (I) varies longitudinally from 50 to 180 km, has low relief with less than 300 m altitude, and is filled with sediments from the Andes, creating several alluvial basins. The second domain (II) is the Andean chain that involves the Western cordillera, with deformed rocks from accreted oceanic crust, and the Eastern cordillera (Cordillera Real) which contains metamorphic rocks from the Paleozoic to Mesozoic (Litherland et al., 1994). Both areas are separated with Tertiary to Quaternary volcanic and volcanoclastic rocks that were deposited in the Interandean Valley. At ~3°S, the Chingual-Cosanga-Pallatanga-Puna (CCPP) fault zone separates the continental plate in two (Alvarado et al., 2016), extending throughout the Puna segment, through the Colombian border and towards Venezuela, creating the North Andean Sliver (NAS) shown in Figure 1. In front of the NAS, the Nazca Plate is less than 26 Ma old (Lonsdale, 2005) and subducts at a relative rate of about 46 mm/yr (Chlieh et al., 2014). More specifically, if we consider the coseismic slip derived by Nocquet et al. (2017) and the aftershock activity analyzed by Agurto-Detzel et al., (2019), the area affected by the Pedernales earthquake extends from Esmeraldas canyon in the north (~1.5°N), down to La Plata area in the south (~1°S). In this segment, the depth of the trench varies from 3.7 km in the north to 2.8 km at the crest of the CR (Collot et al 2004) in the south. Moreover, the oceanic crust thickness shows an along strike variation from 5 km in the north to 14 km in the south, reaching its maximum of 19 km beneath the crest of the CR (Meissner et al., 1977; Calahorrano, 2001; Sallares and Charvis, 2003; Sallares et al., 2005; Graindorge et al., 2004; Garcia Cano et al., 2014).

2.2 The Pedernales earthquake and its aftershocks

On April 16th, 2016, the Mw 7.8 Pedernales earthquake occurred in the central coast of Ecuador, close to the city of Pedernales. This estimated event focal depth is 20 km (Nocquet et al., 2017) and the rupture is characterized as a thrusting mechanism consistent with the megathrust on the plate interface. The Pedernales earthquake ruptured an estimated area of 100 km x 40 km (Nocquet et al., 2017) and propagated along strike from north to south. Although there are different rupture areas proposed for the 1906 earthquake (e.g. Kanamori and McNally, 1982; Yoshimoto et al., 2017), the edges of the 2016 mainshock appear to coincide with the southern boundaries of the 1906 earthquake. This segment of the subduction zone last ruptured in a Mw 7.8 earthquake in 1942. At the southern limit,

the rupture coincides with the northern edge of the 1998 Mw 7.1 earthquake in Bahia Caraquez. The Pedernales earthquake affected an area where large megathrust earthquakes, with magnitudes greater than 7, occurred in the past. Its occurrence correlates with a locked area of interseismic coupling (Chlieh et al., 2014; see Figure 1).

3. NETWORK AND DATA PROCESSING

3.1 THE SEISMIC AFTERSHOCK NETWORK

Immediately after the 2016 Pedernales mainshock, an international collaboration of several institutions including; IGEPN from Ecuador, the French Centre d'études et d'expertise sur les risques, l'environnement, la mobilité et l'aménagement (CEREMA) and GEOAZUR institutes, Lehigh University and University of Arizona from the United States and the University of Liverpool from the United Kingdom, coordinated a rapid response effort to deploy a temporary seismic array. One month after the Pedernales earthquake, we deployed a dense temporary seismological array of broadband and short period seismic stations equally distributed inland along the area affected by the aftershocks (Meltzer et al, 2019). Ocean Bottom Seismometers (OBS) were installed along the trench to complement the stations deployed on land. Figure 2 shows the spatial distribution of the full array including both temporary and permanent stations consisting of more than 80 stations with a station spacing of approximately 10-30 km. The RENSIG Ecuadorian network is a mix of diverse instrumentation including CMG-3ESP, Trillium compact, Trillium 120p, L4C, TSM-1 Strong Motion instruments. The temporary array consists of: (i) short period Lennartz LE 3D Lite recording at 100 Hz; (ii) intermediate period seismometers CMG-40T recording at 200 Hz; (iii) broadband stations Trillium Compact, Guralp CMG-3T and STS-2 recording at 100 Hz. The temporary array was fully operative from May 2016 to June 2017. OBSs were recording between mid-May to November in 2016, at 100 Hz.

3.2 DATA PROCESSING

3.2.1 Onset detection

Based on the initial catalogue provided by IGEPN (http://www.igepn.edu.ec/solicitud-de-datos) with 1677 reported seismic events between May 15th and August 26th, 2016, we created a high quality dataset to be used for the 1D inversion process. We first selected

aftershocks with local magnitude (M_L) greater than 3.5 located in the vicinity of the temporary array. From this catalogue, P- and S-wave arrival times were manually picked for 345 aftershocks using the Seismic Data Explorer (SDX) software package (http://doree.esc.liv.ac.uk:8080/sdx). The events were located based on an average 1D velocity model derived from Font et al. (2013); SDX utilizes a modified hypo71 algorithm for hypocenter location (Lee et al., 1972). Following the procedures from Agurto et al. (2012) and Hicks et al. (2014), we assigned pick error categories, referred as weights, from 0 to 4 to describe the quality of the selected arrival times. Each weight corresponds to the following time uncertainties: Weight 0 (< 0.04 s); Weight 1 (0.04 – 0.1 s); Weight 2 (0.1 – 0.2 s); Weight 3 (0.2 – 1 s); Weight 4 (> 1 s).

3.2.2 Minimum 1D model

From the manually picked catalogue, we further filter to ensure only the highest quality events remain for the minimum 1D velocity model inversion. We selected earthquakes with at least 10 P- and 10 S-onset observations and an azimuthal gap < 200°. In total we obtained a dataset of 227 events with an average of 21 and 17 P- and S-onset times respectively, which contains 4939 P-phases and 3931 S-phases (See Supplementary Material 2).

To minimize the influence of strong topography changes and avoid bias due to the depth of the OBSs, we followed the strategy described by Husen et al. (1999) and Hicks et al. (2014) and set station elevation equal to zero. Station correction terms therefore account for both, the relative elevation and the site-specific velocity differences. Station correction terms were strongly damped (damping = 1000) during the Vp inversion, allowing for greater initial exploration of the Vp parameter space. For the Vs inversion, the damping was decreased (damping = 20), this allows the station-delay terms to absorb errors due to the velocity fluctuations near the stations.

We selected five starting models (see Supplementary Material 3) to cover a wide range of plausible cases: (1) the average model derived from Font et al. (2013), selected as it covers our entire study area with a 3D regional model, (2) an average offshore model based on previous studies by Gailler et al., (2007) and Agudelo et al., (2009), and (3-5) modified versions of the ASW model, used by IGEPN (Font et al., 2013). For models 3-5, we vary the Moho depth between the range of 40 to 60 km. To cover the entire range of feasible velocity models, we created 1000 random variations of each reference velocity model,

sampling from a uniform distribution with bounds ± 0.5 km/s of the reference model velocity. We, therefore, explore 5000 starting models in total, derived from the five classes of models. From the 5000 starting models, the P-wave velocity model with the lowest overall misfit to the travel time picks (RMS 0.335 s) is assumed as our best Vp representation. The density plots in Figure 3d and Figure 3e demonstrate how the best 200 solutions for the inverted Vp and Vs models have a clear convergence towards the best solution between 7.5 km and 40 km depth. The shallowest layers (down to 7.5 km) do also exhibit a convergence towards a minimum velocity solution, however, due to a lack of events occurring in this region, the solution shows a slightly wider range of possible velocities. For the deeper layers (> 40 km), absolute velocities cannot be constrained due to the lack of data and therefore several cluster of solutions can be observed. To detect picking outliers and to estimate an average Vp/Vs ratio for the region, we performed Wadati analysis (Wadati, 1933), displayed in Figure 3a. Onset times show a clear trend for (ts – tp) as a function of tp, a linear trend fit provides a Vp/Vs ratio value of 1.82. A reduced Wadati diagram was also used to have a better control on the outliers in our dataset. Onsets greater than 2σ from the Vp/Vs trend were removed (see Figure 3b). The final dataset of arrival times is represented in a histogram in Figure 3c with a mean of ts-tp of 0.01 s and a variance of 0.70 s^2.

Finally, using our best Vp model and the Vp/Vs ratio (1.82) obtained via Wadati analysis, we built an initial 1D S-wave velocity model. The inversion for the optimum S-wave velocity model follows the same procedure as for the P-wave velocity model. We perturbed the S-wave velocities of the starting model within a range of ± 0.5 km/s, creating 1000 models where both P- and S-phases were simultaneously inverted for. In this step, we fixed the Vp velocities to avoid changes in the previously obtained Vp model by S-wave observations. The solution with the lowest RMS (0.303 s) was accepted as our final S-wave model along with the final set of station corrections and hypocentral locations. By using a Monte Carlo approach for selecting the starting model, we mitigate the dependency of the final model from starting model as we sample a much larger model space.

3.2.3 Regional Moment Tensors

A significant portion of the aftershocks are related to the megathrust faulting displaying reverse solutions consistent with the slip of the plate interface (Agurto-Detzel et al., 2019). We focus our RMT analysis on the seismicity recorded throughout offshore Bahia Caraquez and Cabo Pasado which exhibits various faulting mechanisms. In this area, we observe events distributed close to the trench (5 km – 10 km), however, due to the trade-off between hypocentral depth and origin time, depth location uncertainties in this region are larger than the average. These events could, therefore, be located at the interface, in the upper or in the downgoing plate. To better constrain the focal depth parameter for events in this region, we calculated RMT solutions for 14 events by performing a full waveform inversion using the *isola* package (Sokos et al., 2008; Sokos et al., 2013). We analyzed events reported by IGEPN with local magnitude (M_L) greater than 4.0. The location was fixed to the epicentral locations obtained from our relocation process with VELEST, and the depth is allowed to vary. Green's functions are calculated from a simplified version of our minimum 1D model where the shallowest 8 layers are merged into 4 layers (see Supplementary Material 4). Seismic records were bandpass filtered between 0.04 and 0.09 Hz before the inversion, and between 4 to 10 broadband stations were used for the inversion process of each event.

4. RESULTS

Our final minimum 1D model, represented by 12 layers, with P- and S-wave velocities and the Vp/Vs ratio are given in Table 1 and shown in Figure 4. The model is well constrained between 7.5 km and 40 km, where most of the seismicity is concentrated (see Figure 4). Although, most of the ray paths are concentrated in the shallower layers, we observe some rays down to 40 km depth, which help us to constrain the average of the oceanic and continental Moho depth. At shallower depths, the lack of crustal events (< 7.5 km depth) means we are not able to obtain reliable absolute velocities due to the trade-off with station corrections; at greater depths (30 km – 40 km) the ray path distribution still shows rays passing through, however at depths > 40 km the limited extend does not allow a robust estimation of the average velocities.

The obtained model shows a Vp that fluctuates between 4.45 km/s and 5.04 km/s, in the top layers (down to 7.5 km). From 7.5 km depth to 25 km, Vp consistently increases from 6.3 km/s to 6.6 km/s. Between 30 km – 40 km the constant increase of Vp (from 7.37 km/s at 30

km to 8.04 km/s at 40 km) suggests an area of transition from crust to mantle. At 40 km Vp reaches 8.04 km/s, which can be related with continental upper mantle velocities. Finally, the absence of data between 40 km and 60 km depth, does not allow us to resolve the P-wave velocity, so the resulting values are mainly influenced by our reference model derived by Font et al., (2013) (see Figure 4).

Vp/Vs ratio shows a weighted arithmetic mean of 1.82 for the whole model. In the top layers (down to 7.5 km depth) we find a high Vp/Vs ratio that varies from 1.97 to 2.18. At 10 km depth, the Vp/Vs ratio decreases to 1.85 down to 30 km depth where it rises to 1.93. The Vp/Vs ratio is not well resolved at depths greater than 40 km as we do not have enough data to constrain that area (see Figure 4).

Depth (km)	Vp (km/s)	Vs (km/s)	Vp/Vs
-5.00	*4.45*	*2.26*	*1.97*
2.50	*4.65*	*2.32*	*2.00*
5.00	*5.04*	*2.59*	*1.95*
7.50	*6.32*	*2.90*	*2.18*
10.00	*6.32*	*3.42*	*1.85*
15.00	*6.64*	*3.69*	*1.80*
20.00	*6.64*	*3.76*	*1.77*
25.00	*6.65*	*3.80*	*1.75*
30.00	*7.37*	*3.81*	*1.93*
40.00	*8.04*	*4.64*	*1.73*
50.00	*8.24*	*4.64*	*1.78*
60.00	*8.45*	*4.71*	*1.79*

Table 1 Minimum 1D model. Absolute velocities and Vp/Vs ratio are listed in terms of depth.

Statistics for the inversion also show the robustness of our model. Arrival time residuals were classified according to the weights described in the previous section. Histogram plots in Figure 5 indicate that most of the P- (99 %) and S- (88 %) phase picks are classified between weights 0 and 1. For high quality P-wave onsets (weight 0 and 1), the standard deviations of residuals is 0.24 s and 0.26 s, respectively. For the S phase, the deviation varies from 0.48 s, for weight 0, to 0.52 s for weight 1. Observations for each station display residuals with a normal distribution concentrated between -1 to 1 seconds (See Supplementary Material 5). Overall, the obtained catalogue has a variance of 0.084 s^2, which is above the variance based on the accuracy provided by the manual picking of 0.027 s^2 indicating that we are not overfitting our onset time data.

Our new minimum 1D-velocity model was then used to relocate the 227 manually-picked events (See Supplementary Material 6 for comparison with the original locations). To test the accuracy of the resulting hypocenters, we performed a stability test by randomly perturbing hypocenters starting locations by between 7.5 km – 12.5 km in latitude, longitude and depth. We then relocated the events using our minimum 1-D velocity model and station corrections. The location of the recovered seismicity shifts only marginally respect to the original positions, leading to an estimation of the relocation uncertainties around 1 km in latitude and longitude, and 2.7 km in depth (See Supplementary Material 7). Overall, the relocated seismicity displays an average error of 1.38 km and 1.57 km for the horizontal and vertical component, respectively. As hypocentral uncertainty is shown to increase with distance offshore, we separately calculate the location errors for the offshore seismicity. For this data subset, we obtain average uncertainties of 1.53 km for the horizontal axis and 2.15 km for the vertical axis.

The relocated aftershocks are shown in Figure 6. The seismicity is distributed between 5-10 km to 100 km eastward of the trench and between 2 km to 35 km in depth. The most important features are as follows:

(1) We observe that our epicentral distribution for the analyzed aftershocks are in agreement with other related studies (e.g. Meltzer et al., (2019), Agurto-Detzel et al., (2019)). We find that events with local magnitude greater than 3.5 are generally distributed outside the coseismic slip area of the 2016 Pedernales mainshock and skew towards the trench.

(2) Most of the seismicity along profiles AA’ and BB’ is located along the plate interface. Slab1.0 (Hayes et al., 2012) is used as a reference in Figure 6, however a comparison between both Slab1.0 (Hayes et al., 2012) and Slab2.0 (Hayes et al., 2018) is shown in Supplementary Material 8. The northern profile AA’ demonstrates the differences between the interface for both models, in the region, Slab2.0 is relatively deeper than the Slab1.0 interface; the located aftershocks are distributed between both Slab1.0 and Slab2.0. These relative changes in extensively used slab models further highlight the complexities the Ecuadorian margin along strike.

(3) Clustered activity in the overriding plate can be observed in both northern (AA’) and southern (BB’) profiles.

(4) Profiles AA’ and BB’ (see Figure 6) show that a portion of the aftershocks reach the trench. This has been demonstrated as a robust feature due to specific bias testing of the offshore relocated seismicity.

Although, the formal locations errors stated before are less than 3 km in depth, absolute locations errors can be significantly larger. To identify whether the events distributed close to the trench are located in the subducting or the overriding plate, we calculated RMT solutions to better constrain the hypocenter depth. We focus here on the offshore seismicity located close to profile BB’ and calculated 14 RMTs. This is an area where Agurto-Detzel et al. (2019) reported a single anomalous strike-slip event at about 10 km depth. Figure 6 shows the solutions superimposed over the relocated aftershock activity. Additional information about the waveform inversion fit and comparison with other MT catalogues are shown in Supplementary Material 9, 10 and 11. We also compare the difference between depths obtained from the velocity model inversion and isola. Events with depths between 5 km and 15 km, based on arrival times, show a small difference in their depth locations in comparison to the RMT solutions. For the offshore seismicity located with depths > 15 km using travel times, the RMT centroid depths are shallower than those of the hypocenters (see Table 2 and Supplementary Material 12 and 13).

The majority of the aftershock RMTs for the Pedernales segment exhibit a thrust mechanism related to the subduction interface (e.g. Agurto-Detzel et al., 2019). However, we also find events that display extensional and strike slip faulting mechanisms, distributed along the marine forearc. Table 2 summarizes our results listing the centroid information, nodal planes, magnitude, variance reduction and double-couple percentage.

#	Lat (°)	Lon (°)	Centroid depth (km)	Arrival times depth (km)	Strike	Dip	Rake	Mag (Mw)	Var (%)	DC (%)	ID	Date
1	*0.6330*	*-80.2077*	*13.00*	*8.24*	*196*	*72*	*94*	*4.4*	*80*	*82.3*	*e0*	*2016-06-06 16:45:08*
2	*0.2940*	*-80.5730*	*2.03*	*4.42*	*342*	*57*	*-79*	*5.1*	*68*	*89.5*	*e3*	*2016-06-01 10:05:16*
3	*0.3740*	*-80.4910*	*14.03*	*11.91*	*174*	*60*	*65*	*4.4*	*86*	*61.2*	*e4*	*2016-05-31 15:48:11*
4	*0.1295*	*-80.1691*	*25.03*	*25.53*	*173*	*84*	*81*	*3.3*	*28*	*63.8*	*e5*	*2016-05-30 05:48:56*
5	*-0.2000*	*-80.5770*	*5.00*	*18.37*	*290*	*54*	*-66*	*3.3*	*13*	*71.1*	*e7*	*2016-06-21 04:40:24*
6	*-0.2718*	*-80.6639*	*16.03*	*12.54*	*49*	*49*	*164*	*3.7*	*13*	*31.5*	*e8*	*2016-06-02 00:18:59*
7	*-0.1880*	*-80.6652*	*16.03*	*18.99*	*175*	*74*	*74*	*3.5*	*44*	*62.5*	*e9*	*2016-06-01 02:12:22*
8	*-0.4079*	*-80.9864*	*14.02*	*8.14*	*247*	*88*	*177*	*3.8*	*45*	*76.0*	*e14*	*2016-07-07 17:10:13*
9	*-0.4444*	*-80.9390*	*8.03*	*29.99*	*143*	*74*	*-27*	*3.9*	*18*	*99.1*	*e16*	*2016-07-08 04:41:34*
10	*-0.4268*	*-80.8981*	*12.03*	*7.88*	*316*	*89*	*24*	*4.6*	*66*	*55.6*	*e17*	*2016-07-08 07:03:48*
11	*-0.4047*	*-80.9177*	*12.03*	*22.99*	*316*	*86*	*29*	*4.2*	*61*	*43.3*	*e18*	*2016-07-08 07:35:15*
12	*-0.2629*	*-80.8675*	*10.03*	*22.35*	*324*	*50*	*28*	*4.0*	*57*	*10.4*	*e19*	*2016-07-10 06:44:34*
13	*-0.1967*	*-80.9427*	*8.03*	*-*	*250*	*80*	*35*	*4.2*	*23*	*70.0*	*e25*	*2016-05-05 16:06:40*
14	*0.3242*	*-80.6818*	*2.03*	*4.16*	*318*	*61*	*-110*	*4.7*	*57*	*65.9*	*e27*	*2016-06-01 15:00:51*

Table 2 summary of results for the obtained RMT. Depths calculated based on arrival times inversion were included for comparison.

5. DISCUSSION

5.1 Velocity Model

Figure 4 shows the best 1D velocity model. The histograms show depth distribution of the aftershock seismicity and help to demonstrate the resolution of our model at different depths. Although a more in-depth interpretation requires at least a 2D velocity model, our obtained 1D velocity model allows us to observe and discuss depth ranges and to first order the velocity structure with depth. High Vp/Vs ratio obtained in the shallow layers can be related to hydrated sediments, non-consolidated soils and/or fractured oceanic crust (Peacock, 2001; Hacker et al., 2003; Kato et al., 2010; Pasten-Araya et al., 2018). The values in this section (up to 2.2 at 7.5 km depth) may reflect an upward migration of fluids coming from the dehydration of sediments subducting within the Nazca plate. Similar cases have been discussed in other areas such as northern Chile (Husen et al., 2001), New Zealand (Barnes et al., 2009), Sumatra (Collings et al., 2012) and Costa Rica (Bangs et al., 2015). As we are dealing with P- and S- onsets coming from both OBS and inland stations, in the depth range between 10 km and 40 km, the subduction process of the Nazca plate descending beneath the South American plate produces an overlapping of velocities from both plates

which do not allow us to address each plate individually in a one-dimensional model. However, there is a constant increase in velocities for both P- and S-wave indicating more consolidated rocks. We also identify another increase in the Vp/Vs ratio (Vp/Vs = 1.90) around 30 km depth. A change in Vp/Vs ratio at ~30km depth agrees with the findings of Hacker et al. (2003) and Bloch et al. (2018) who associated these characteristics with the dehydration of the subducting oceanic plate. Between 30 km – 40 km it is not possible to observe a sharp contrast. However, due to the rapid increase of Vp we suggest a transitional area where the oceanic Moho could be located. At depths greater than 40 km, Vp reaches values > 8 km/s that can be associated with velocities of the upper mantle (Gailler et al., 2007; Font et al., 2013; Araujo, 2016).

Station correction terms were also calculated in the inversion. Figure 8 shows the delays obtained for both P- and S-wave onsets. EC16 was used as a reference station because of its central location along the array and large number of observations (total= 384, P= 214, S=170). For the P-delay times, the standard deviation for all stations shows that values are concentrated around 0.50 s. Delays for the S phase show a distribution around 0.85 s. In both cases, the obtained values are coherent within the study region following a west to east change of sign that moves from negative to positive. This change is mainly associated with two factors: (1) The eastward dipping of the subducting Nazca plate that produces large residuals in the inversion as VELEST maps the 2D structure into the station correction terms; (2) the variations in topography of the area, from around 3000 meters below sea level at the trench to 700 meters above sea level in the coastal range. If we consider the difference in elevation of the array, a geological interpretation will only be valid for the inland stations as the reference station (EC16) is located in this area, and the delay in the OBS can mainly be explained due to the abrupt changes in topography from sea level to the trench (~ 4000 m depth).

Taking this into account, the difference in elevation for the inland seismic stations range from sea level for stations installed close to the coast to 688 m for the stations deployed at the base of the coastal range. Station correction terms in Figure 8, especially for the S-phase, show a NE-SW variation in sign from negative to positive which might be related with changes in the geological conditions of the area. Those changes coincide with the Jama Fault System (JFS) mapped in coastal Ecuador (Reyes and Michaud, 2012) and can be attributed to

differences in the properties on both sides of the fault. Along the coast, it is possible to find Cretaceous formations (~89 Ma, Luzieux et al., 2006) with rocks from the oceanic crust that were accreted onto the margin and could explain the negative delay in station terms. To the east side of the JFS, less consolidated formations such as conglomerates, volcanic sediments and alluvial formations from the Miocene, Pliocene and Quaternary, respectively, were mapped (Bristow and Hoffstetter, 1977; Cantalamessa et al., 2005; Cantalamessa et al., 2007) and can be correlated with the positive delay observed in our inversion. This difference in the geological structures is also consistent with the observation that cities far from the epicenter (> 100 km) suffered severe damage due to site effects such as Portoviejo and Chone where the vertical component of PGA reached up to 1.01 m/s^2 and 1.72 m/s^2 (IGEPN, 2016) and the delay terms for the S-phase calculated were 2.08 s and 2.57 s, respectively. The role of the fault system in the seismicity of the Central Coastal Ecuadorian margin will be discussed in detail in the next section.

5.2 Aftershocks distribution

The majority of our relocated events with local magnitude greater than 3.5 are surrounding the coseismic slip area determined by Nocquet et al (2017). This type of aftershock distribution concentrated on the updip part of the rupture has been previously observed in other megathrust earthquakes along the South American margin such as the Mw 8.8 Maule 2010 earthquake (Rietbrock et al., 2012) and the Mw 8.2 Iquique earthquake (Leon-Rios et al., 2016).

The distribution of our relocated aftershocks along the margin are consistent with the observations from Meltzer et al. (2019), Agurto-Detzel et al. (2019) that show seismicity streaks aligned perpendicular to the trench (see Supplementary Material 14). The seismicity distribution during the interseismic cycle (Font et al., 2013) is similar to the aftershock sequence of the Pedernales earthquake and suggests that this behavior could be a regular feature of the Ecuadorian subduction zone (see Supplementary Material 14).

Cross sections AA’ and BB’, in Figure 6, show that the depth distribution of the events is consistent with Slab1.0 from Hayes et al. (2012). While the northern section is in a good agreement with the projection of the slab at distances greater than 50 km eastward from

the trench, the southern profile shows seismicity that could indicate a shallower plate interface (see profile BB' in Supplementary Material 8). The subduction of the CR helps to explain this distribution due to the addition of a more buoyant oceanic crust which causes the raising of the seismogenic interface zone. This has been previously proposed by Collot et al. (2004) and Gailler et al. (2007) using active seismic methods in the forearc region of the Ecuadorian margin.

It is also possible to identify clustered seismicity in both sections, north and south, that are located in the overriding plate. This type of activity might be caused by the activation of crustal faults due to changes in Coulomb stress in the area surrounding the coseismic slip (e.g. Ryder et al., 2012).

As previously mentioned, the aftershock seismicity, located in the northern profile AA', occurs very close to the trench, up to ~5 km – 10 km, which we confirmed using the OBS stations offshore. Usually, seismicity along subduction margins does not extend up to areas close to the trench axis. Although this phenomena has been previously observed when an accretionary prism is present in the subduction zone, even in a erosional regime it is uncommon to observe seismicity with such proximity to the trench (i.e. 2010 Maule, Chile (Rietbrock et al., (2012); Lange et al., (2012); 2015 Mw 8.3 Illapel, Chile (Ruiz et al., 2016); 2014 Mw 8.2 Iquique, Chile (Leon-Rios et al., 2016); New Zealand (Anderson & Webb, 2010); Japan (Asano et al., 2011)). This activity might be related to (1) intraplate deformation due to the bending of the oceanic crust that can causes seismicity in the subducting slab and/or to (2) the absence of a frontal accretionary prism that allows the locking of the megathrust to extend up to the trench, causing seismicity, even at shallow depths.

Finally, the presence of subducting seamounts acting as erosional agents, helps to create a scenario which might promote locking and allow seismicity to extend up to the trench along zones of weakness activated after large earthquakes.

5.3 Deformation in the marine forearc and upper crust

Previous studies by Agurto-Detzel et al., (2019) and Meltzer et al., (2019) have described the overall deformation caused by the Pedernales earthquake. As we now have developed a robust minimum 1D model for the area affected by the 2016 mainshock and also manually determined high precision onset times, we are able to constrain the hypocentral depths in

greater detail. We, therefore, will concentrate our discussion on the offshore area close to Cabo Pasado (see Figure 7) and analyze the deformation in the marine forearc and upper crust based on the diverse seismicity found in this area. The distribution and mechanisms of the 14 calculated RMTs in this study are superimposed over our event locations in Figure 6. Thrusting focal mechanisms from the gCMT catalogues (Esktrom et al., 2012) are also shown and highlight the diversity of our obtained solutions.

In profile AA' we found two events with extensional components (e3 and e27 in Table 2) occurring in the overriding plate. Our RMT solutions agree with the suggestion by Marcaillou et al. (2016) who proposed that seamounts, part of the Atacames chain, could cause the activation of normal faults in the marine forearc of the overriding plate. Normal faulting in the marine forearc has been previously observed in the South American margin (Ruiz et al., 2014), especially in areas within erosive regime like in central Ecuador, where the overriding plate contains a small accretionary prism and a fractured, eroded and hydrated wedge that is easy to break.

Across profile BB', we observed a clear pattern of strike-slip mechanisms distributed along the marine forearc (near the plate interface) and surrounding the scarps in front of Cabo Pasado. This strike-slip sequence lasted for two days between the 7th and 8th July 2016. Figure 7 shows in detail the distribution of those events. This type of seismic activity in the area has been previously observed by Vaca et al., (2017, fig 2.7) close to La Plata island (~ 1°S).

Reactivation of preexisting normal faults in the upper crust after large megathrust earthquakes has been recently observed in many subduction zone settings (i.e. Farias et al.,2011, Ryder et al., 2012, Asano et al., 2011, Kato et al., 2011, Toda et al., 2013). Although normal fault mechanisms are also detected for the Pedernales aftershock sequence we observe a considerable amount of strike-slip seismicity that might be related to the following possible causes:

(1) The pattern followed by the strike-slip events is consistent with the projection of the crest of the CR derived by Pilger, 1984 (see Figure 7). Around 80 km to the north of the CR, the forearc was affected by the subduction of the Atacames seamounts (Collot et al., 2005; Marcaillou et al., 2016) causing deformation on the margin and creating two scarps of 25 to 40 km wide separated by a shallow promontory (Collot et al., 2009) (see Figure 7). This

suggests that subduction of the CR beneath the South American plate might create large scale deformation and reactivate transform faulting in the overriding plate.

(2) The location of the offshore Cabo Pasado seismicity is coincident with a rotational block system proposed by Daly (1989) that extends along the whole Pedernales segment. This system was created 45 Ma ago in the Mid-Late Eocene because of the rapid convergence rate between the Nazca and the South American plates. The interaction of the two convergent plates plus the presence of a major shear fault could have caused faulting in the forearc between the trench and the coast, creating several independent blocks in the Pedernales segment. Rapid changes in the relative velocities of these blocks could have caused both faults and blocks to have been rotated within the bounding shear zones, generating zones of strike-slip faulting at the edges of each block. These features remained inactive after the stabilization of convergence from the Late Miocene (~10 Ma) to the present day. Possible reactivation of the strike-slip faults might be related to the occurrence of large megathrust earthquake.

(3) Seismicity is associated with the possible extension offshore of the Jama Fault System (JFS) that also coincides with the area where the crest of the CR is located. The JFS could be explained as a large-scale system that was generated to release the stress accumulated by the interaction between the CCPP fault zone and the convergence margin. Collot et al., (2004) proposed the JFS as an active transcurrent fault that extends offshore which was confirmed by Hernandez et al., (2011) and Michaud et al., (2015). It is possible that the occurrence of a large megathrust earthquake triggered the nucleation of seismicity along this fault.

In our opinion, a combination between hypothesis (1) and (3) is most likely to explain the observed activity because large-scale strike-slip system as the JFS normally do not extend in one single line but in several strands, covering an entire region as has been observed inland for the same system. In addition, the interaction between the CR and the upper crust where the JFS extends might contribute to the generation of this type of seismicity. These two factors, in addition to a large megathrust earthquake, such as the 2016 Pedernales event, could have provided the conditions to reactivate a strike-slip fault in the marine forearc. This offshore feature might have an important role as a barrier for large megathrust

595 earthquakes by absorbing the stress released during the reverse coseismic and transform it
596 into strike-slip displacement (e.g. Collot et al., 2004).

597 Whatever the cause is, the occurrence of seismicity associated with the reactivation of a
598 strike-slip fault in the marine forearc is a remarkable observation. Upper crustal activity,
599 related to normal faulting has been often documented: e.g. Pichilemu in central Chile (Farías
600 et al, 2011; Ryder et al., 2012) and also in Japan (Kato et al., 2011). It is therefore interesting
601 to note that strike-slip faults can also be reactivated and should, therefore, be mapped in
602 order to update the hazards map in the region.

603

604 6. CONCLUSIONS

605 We inferred a minimum 1D model for the Pedernales segment based on the aftershock
606 sequence (M_L > 3.5) of the Mw 7.8 Pedernales earthquake. The velocity structure for both P-
607 and S-phases was obtained after manually picking 345 events recorded by the permanent
608 Ecuadorian seismic network and a temporary array that includes more than 70 inland and
609 marine stations installed one month after the mainshock. P- and S- arrival times from 227
610 earthquakes with gap < 200° were inverted with VELEST to obtain absolute velocities,
611 hypocentral locations and station correction terms.

612 The obtained minimum 1D velocity model shows a good resolution down to 40 km depth
613 constrained with the ray paths and the earthquake distribution. The area has an average
614 Vp/Vs ratio of 1.82 which varies with depth that may be related to hydration and
615 serpentinization in the downgoing plate.

616 The seismicity is distributed in streaks which align perpendicular to the trench. Cross
617 sections allow us to identify the seismogenic contact between the Nazca and South
618 American plates. Shallow seismicity was observed in both northern and southern segments
619 of the rupture area suggesting the activation of faults in the overriding plate. Some of the
620 observed seismicity reached the trench which suggests the absence of a frontal accretionary
621 prism.

622 Regional moment tensors were calculated to analyze the source mechanism of some events
623 offshore. Although the majority of the events show focal mechanisms consistent with the
624 subduction process, we also observe extensional faulting in the marine forearc that can be

associated to the subduction of already-mapped seamounts. We also found strike-slip faulting which might be related to the reactivation of a strike-slip structure after the 2016 Mw 7.8 Pedernales earthquake that, in combination with the subduction of the crest of the CR, might cause the nucleation of the observed seismicity along the marine forearc margin. The observation of this type of activity suggests the need to reevaluate the geological structures in the marine forearc and to update the seismic hazard map for this region including the possible scenario of a large strike-slip event.

6. ACKNOWLEDGMENTS

This study was supported by IGEPN, IRD, the INSU-CNRS and the ANR grant ANR-15-CE04-0004. The UK portion of the temporary deployment was supported by NERC grant NE/P008828/1. The US portion of the temporary deployment was supported by IRIS PASSCAL and NSF RAPID Program Award EAR-1642498. SLR acknowledges partial support from Programa Formacion de Capital Humano Avanzado, BECAS DE DOCTORADO EN EL EXTRANJERO, BECAS CHILE (Grant 8068/2015). HAD acknowledges support from ANR project ANR-15-CE04-0004 and UCA/JEDI project ANR-15-IDEX-01.

We are also indebted to Ben Yates, Davide Oregioni and Deny Malengros from Geoazur laboratories, INOCAR, Comandante Andrès Pazmino (INOCAR) and Captain Patricio Estupinian (Esmeraldas Coastguard) to operate OBSs at sea in very harsh environments.

Authors want to thanks to all involved in the deployment and data collection for his invaluable collaboration with this study. Finally, to all the people in Ecuador who allowed us to install our stations in their houses, big thanks for your hospitality, patience and help when was needed.

References (APA)

Abe, K. (1979). Size of great earthquakes of 1837–1974 inferred from tsunami data. *Journal of Geophysical Research: Solid Earth*, *84*(B4), 1561-1568.

Agudelo, W., Ribodetti, A., Collot, J. Y., & Operto, S. (2009). Joint inversion of multichannel seismic reflection and wide-angle seismic data: Improved imaging and refined velocity

654 model of the crustal structure of the North Ecuador–South Colombia convergent margin.
655 *Journal of Geophysical Research: Solid Earth*, *114*(B2).

656 Agurto-Detzel, H., Font, Y., Charvis, P., Rietbrock, A., Ambrois, D., Paullato, M., … Soto-
657 Cordero, L. (2019). Ridge subduction and afterslip control aftershock distribution of the
658 2016 Mw 7.8 Ecuador earthquake. *Earth and Planetary Science Letters*.

659 Agurto, H., Rietbrock, A., Barrientos, S., Bataille, K., & Legrand, D. (2012). Seismo-tectonic
660 structure of the Aysén Region, Southern Chile, inferred from the 2007 M w= 6.2 Aysén
661 earthquake sequence. *Geophysical Journal International*, *190*(1), 116-130.

662 Alvarado, A., Audin, L., Nocquet, J. M., Jaillard, E., Mothes, P., Jarrín, P., ... & Cisneros, D.
663 (2016). Partitioning of oblique convergence in the Northern Andes subduction zone:
664 Migration history and the present-day boundary of the North Andean Sliver in Ecuador.
665 *Tectonics*, *35*(5), 1048-1065.

666 Alvarado, A., Ruiz, M., Mothes, P., Yepes, H., Segovia, M., Vaca, M., ... & Aguilar, J. (2018).
667 Seismic, volcanic, and geodetic networks in Ecuador: Building capacity for monitoring and
668 research. *Seismological Research Letters*, *89*(2A), 432-439.

669 Anderson, H., & Webb, T. (1994). New Zealand seismicity: patterns revealed by the
670 upgraded National Seismograph Network. *New Zealand journal of geology and geophysics*,
671 *37*(4), 477-493.

672 Araujo, S. (2016). *Travel time tomography of the crust and the mantle beneath Ecuador from*
673 *data of the national seismic network* (Doctoral dissertation, Grenoble Alpes).

674 Asano, Y., Saito, T., Ito, Y., Shiomi, K., Hirose, H., Matsumoto, T., ... & Sekiguchi, S. (2011).
675 Spatial distribution and focal mechanisms of aftershocks of the 2011 off the Pacific coast of
676 Tohoku Earthquake. *Earth, planets and space*, *63*(7), 29.

677 Bangs, N. L., McIntosh, K. D., Silver, E. A., Kluesner, J. W., & Ranero, C. R. (2015). Fluid
678 accumulation along the Costa Rica subduction thrust and development of the seismogenic
679 zone. *Journal of Geophysical Research: Solid Earth*, *120*(1), 67-86.

680 Barnes, P. M., Lamarche, G., Bialas, J., Henrys, S., Pecher, I., Netzeband, G. L., ... & Crutchley,
681 G. (2010). Tectonic and geological framework for gas hydrates and cold seeps on the
682 Hikurangi subduction margin, New Zealand. *Marine Geology*, *272*(1-4), 26-48.

683 Beck, S. L., and L. J. Ruff (1984). The rupture process of the great 1979 Colombia
684 earthquake: Evidence for the asperity model, *J. Geophys. Res*., 89, 9281-9291.

685 Beauval, C., Yepes, H., Bakun, W. H., Egred, J., Alvarado, A., & Singaucho, J. C. (2010).
686 Locations and magnitudes of historical earthquakes in the Sierra of Ecuador (1587–1996).
687 *Geophysical Journal International*, *181*(3), 1613-1633.

688 Bilek, S. L. (2010). Invited review paper: Seismicity along the South American subduction
689 zone: Review of large earthquakes, tsunamis, and subduction zone complexity.
690 *Tectonophysics*, *495*(1-2), 2-14.

691 Bloch, W., John, T., Kummerow, J., Salazar, P., Krüger, O. S., & Shapiro, S. A. Watching
692 Dehydration: Seismic Indication for Transient Fluid Pathways in the Oceanic Mantle of the
693 Subducting Nazca Slab. *Geochemistry, Geophysics, Geosystems*.

694 Bolton, P. A. (1991). Local Level Economic and Social Consequences. *The March 5, 1987,*
695 *Ecuador earthquakes: mass wasting and socioeconomic effects*, 100.

696 Bristow, C. R., Hoffstetter, R., Feininger, T., & Hall, M. T. (1977). Léxico estratigráfico del
697 Ecuador. *CENTRE NATIONAL DE LA RECHERCHE SCIENTIFIQUE*.

698 Calahorrano, A. (2001). *Estudio del origen del enjambre sısmico de la zona norte de la ciudad*
699 *de Quito, durante 1998–99. Escuela Politécnica Nacional, Facultad de Geologıa, Minas y*
700 *Petróleos* (Doctoral dissertation, Tesis de Ingeniera Geóloga, Quito, Ecuador).

701 Calahorrano, A., Sallarès, V., Collot, J. Y., Sage, F., & Ranero, C. R. (2008). Nonlinear
702 variations of the physical properties along the southern Ecuador subduction channel:
703 Results from depth-migrated seismic data. *Earth and Planetary Science Letters*, *267*(3-4),
704 453-467.

705 Cano, L. C. G., Galve, A., Charvis, P., & Marcaillou, B. (2014). Three-dimensional velocity
706 structure of the outer fore arc of the Colombia-Ecuador subduction zone and implications
707 for the 1958 megathrust earthquake rupture zone. *Journal of Geophysical Research: Solid*
708 *Earth*, *119*(2), 1041-1060.

709 Cantalamessa, G., & Di Celma, C. (2005). Sedimentary features of tsunami backwash
710 deposits in a shallow marine Miocene setting, Mejillones Peninsula, northern Chile.
711 *Sedimentary Geology*, *178*(3-4), 259-273.

712 Cantalamessa, G., Di Celma, C., Ragaini, L., Valleri, G., & Landini, W. (2007). Sedimentology
713 and high-resolution sequence stratigraphy of the late middle to late Miocene Angostura
714 Formation (western Borbón Basin, northwestern Ecuador). *Journal of the Geological Society*,
715 *164*(3), 653-665.

716 Chlieh, M., Mothes, P. A., Nocquet, J. M., Jarrin, P., Charvis, P., Cisneros, D., ... & Vallée, M.
717 (2014). Distribution of discrete seismic asperities and aseismic slip along the Ecuadorian
718 megathrust. *Earth and Planetary Science Letters*, *400*, 292-301.

719 Collings, R., Lange, D., Rietbrock, A., Tilmann, F., Natawidjaja, D., Suwargadi, B., ... & Saul, J.
720 (2012). Structure and seismogenic properties of the Mentawai segment of the Sumatra
721 subduction zone revealed by local earthquake traveltime tomography. *Journal of*
722 *Geophysical Research: Solid Earth*, *117*(B1).

723 Collot, J. Y., Charvis, P., Gutscher, M. A., & Operto, S. (2002). Exploring the
724 Ecuador-Colombia active margin and interplate seismogenic zone. *EOS, Transactions*
725 *American Geophysical Union*, *83*(17), 185-190.

726 Collot, J. Y., Marcaillou, B., Sage, F., Michaud, F., Agudelo, W., Charvis, P., ... & Spence, G.
727 (2004). Are rupture zone limits of great subduction earthquakes controlled by upper plate
728 structures? Evidence from multichannel seismic reflection data acquired across the northern
729 Ecuador–southwest Colombia margin. *Journal of Geophysical Research: Solid Earth*,
730 *109*(B11).

731 Collot, J. Y., Migeon, S., Spence, G., Legonidec, Y., Marcaillou, B., Schneider, J. L., ... &
732 Pazmino, A. (2005). Seafloor margin map helps in understanding subduction earthquakes.
733 *Eos, Transactions American Geophysical Union*, *86*(46), 463-465.

734 Collot, J. Y., Michaud, F., Alvarado, A., Marcaillou, B., Sosson, M., Ratzov, G., ... & Pazmino,
735 A. (2009). Visión general de la morfología submarina del margen convergente de Ecuador-
736 Sur de Colombia: implicaciones sobre la transferencia de masa y la edad de la subducción de
737 la Cordillera de Carnegie. *En Geología y Geofísica Marina y Terrestre del Ecuador*.

738 Collot, J. Y., Sanclemente, E., Nocquet, J. M., Leprêtre, A., Ribodetti, A., Jarrin, P., ... &
739 Charvis, P. (2017). Subducted oceanic relief locks the shallow megathrust in central Ecuador.
740 *Journal of Geophysical Research: Solid Earth*, *122*(5), 3286-3305.

741 Daly, M. C. (1989). Correlations between Nazca/Farallon plate kinematics and forearc basin
742 evolution in Ecuador. *Tectonics*, *8*(4), 769-790.

743 Dorbath, L., Cisternas, A., & Dorbath, C. (1990). Assessment of the size of large and great
744 historical earthquakes in Peru. *Bulletin of the Seismological Society of America*, *80*(3), 551-
745 576.

746 Dziewonski, A. M., Chou, T. A., & Woodhouse, J. H. (1981). Determination of earthquake
747 source parameters from waveform data for studies of global and regional seismicity. *Journal*
748 *of Geophysical Research: Solid Earth*, *86*(B4), 2825-2852.

749 Egred, J. (1968). Breve historia sísmica de la República del Ecuador (1534-1965). *Bol. Bibl.*
750 *Geofís. Oceanogr. Am*.

751 Ekström, G., Nettles, M., & Dziewoński, A. M. (2012). The global CMT project 2004–2010:
752 Centroid-moment tensors for 13,017 earthquakes. *Physics of the Earth and Planetary*
753 *Interiors*, *200*, 1-9.

754 Farías, M., Comte, D., Roecker, S., Carrizo, D., & Pardo, M. (2011). Crustal extensional
755 faulting triggered by the 2010 Chilean earthquake: The Pichilemu Seismic Sequence.
756 *Tectonics*, *30*(6).

757 Font, Y., Segovia, M., Vaca, S., & Theunissen, T. (2013). Seismicity patterns along the
758 Ecuadorian subduction zone: new constraints from earthquake location in a 3-D a priori
759 velocity model. *Geophysical Journal International*, *193*(1), 263-286.

760 Gailler, A., Charvis, P., & Flueh, E. R. (2007). Segmentation of the Nazca and South American
761 plates along the Ecuador subduction zone from wide angle seismic profiles. *Earth and*
762 *Planetary Science Letters*, *260*(3-4), 444-464.

763 Graindorge, D., Calahorrano, A., Charvis, P., Collot, J. Y., & Bethoux, N. (2004). Deep
764 structures of the Ecuador convergent margin and the Carnegie Ridge, possible consequence
765 on great earthquakes recurrence interval. *Geophysical Research Letters*, *31*(4).

766 Hayes, G. P., Wald, D. J., & Johnson, R. L. (2012). Slab1. 0: A three-dimensional model of
767 global subduction zone geometries. *Journal of Geophysical Research: Solid Earth*, *117*(B1).

768 Hacker, B. R., Abers, G. A., & Peacock, S. M. (2003). Subduction factory 1. Theoretical
769 mineralogy, densities, seismic wave speeds, and H2O contents. *Journal of Geophysical*
770 *Research: Solid Earth*, *108*(B1).

771 Hacker, B. R., Peacock, S. M., Abers, G. A., & Holloway, S. D. (2003). Subduction factory 2.
772 Are intermediate-depth earthquakes in subducting slabs linked to metamorphic dehydration
773 reactions?. *Journal of Geophysical Research: Solid Earth*, *108*(B1).

774 Herd, D. G., Youd, T. L., Meyer, H., Person, W. J., & Mendoza, C. (1981). The great tumaco,
775 colombia earthquake of 12 december 1979. *Science*, *211*(4481), 441-445.

776 Hernández, M. J., Michaud, F., Rivadeneira, M., Barba, D., & Collot, J. Y. (2011). El sistema de
777 fallas de Jama en la plataforma continental (off-shore) del margen ecuatoriano: resultados
778 preliminares a partir de la interpretación de perfiles sísmicos de reflexión.

779 Hicks, S. P., Rietbrock, A., Ryder, I. M., Lee, C. S., & Miller, M. (2014). Anatomy of a
780 megathrust: The 2010 M8. 8 Maule, Chile earthquake rupture zone imaged using seismic
781 tomography. *Earth and Planetary Science Letters*, *405*, 142-155.

782 Husen, S., Kissling, E., Flueh, E., & Asch, G. (1999). Accurate hypocentre determination in the
783 seismogenic zone of the subducting Nazca Plate in northern Chile using a combined on-
784 /offshore network. *Geophysical Journal International*, *138*(3), 687-701.

785 Husen, S., & Kissling, E. (2001). Postseismic fluid flow after the large subduction earthquake
786 of Antofagasta, Chile. *Geology*, *29*(9), 847-850.

787 IGEPN, 2016 informe sismico n18, https://www.igepn.edu.ec/servicios/noticias/1324-
788 informe-sismico-especial-n-18-2016

789 International Seismological Centre, *On-line Bulletin*, http://www.isc.ac.uk, Internatl. Seismol.
790 Cent., Thatcham, United Kingdom, 2015.

791 Jaillard, E., Benitez, S., Berrones, G., Huaman, C., Ordonez, M., & Rivadeneira, M. (1994).
792 Analisis de cuencas sedimentarias e historia precoz de los Andes.

793 Jaillard, E., Hérail, G., Monfret, T., Díaz-Martínez, E., Baby, P., Lavenu, A., & Dumont, J. F.
794 (2000). Tectonic evolution of the Andes of Ecuador, Peru, Bolivia and northernmost Chile.
795 *Tectonic Evolution of South America*, *31*, 481-559.

Kanamori, H., & Given, J. W. (1981). Use of long-period surface waves for rapid determination of earthquake-source parameters. *Physics of the Earth and Planetary interiors*, *27*(1), 8-31.

Kanamori, H., & McNally, K. C. (1982). Variable rupture mode of the subduction zone along the Ecuador-Colombia coast. *Bulletin of the Seismological Society of America*, *72*(4), 1241-1253.

Kato, A., Iidaka, T., Ikuta, R., Yoshida, Y., Katsumata, K., Iwasaki, T., ... & Watanabe, T. (2010). Variations of fluid pressure within the subducting oceanic crust and slow earthquakes. *Geophysical research letters*, *37*(14).

Kato, A., Sakai, S. I., & Obara, K. (2011). A normal-faulting seismic sequence triggered by the 2011 off the Pacific coast of Tohoku Earthquake: Wholesale stress regime changes in the upper plate. *Earth, planets and space*, *63*(7), 43.

Kato, A., & Nakagawa, S. (2014). Multiple slow-slip events during a foreshock sequence of the 2014 Iquique, Chile Mw 8.1 earthquake. *Geophysical Research Letters*, *41*(15), 5420-5427.

Kelleher, J. A. (1972). Rupture zones of large South American earthquakes and some predictions. *Journal of Geophysical Research*, *77*(11), 2087-2103.

Kendrick, E., Bevis, M., Smalley Jr, R., Brooks, B., Vargas, R. B., Lauría, E., & Fortes, L. P. S. (2003). The Nazca–South America Euler vector and its rate of change. *Journal of South American Earth Sciences*, *16*(2), 125-131.

Kissling, E., Ellsworth, W. L., Eberhart-Phillips, D., & Kradolfer, U. (1994). Initial reference models in local earthquake tomography. *Journal of Geophysical Research: Solid Earth*, *99*(B10), 19635-19646.

Lange, D., Tilmann, F., Barrientos, S. E., Contreras-Reyes, E., Methe, P., Moreno, M., ... & Beck, S. (2012). Aftershock seismicity of the 27 February 2010 Mw 8.8 Maule earthquake rupture zone. *Earth and Planetary Science Letters*, *317*, 413-425.

Lanning, F., Haro, A. G., Liu, M. K., Monzón, A., Monzón-Despang, H., Schultz, A., ... & Vera-Grunauer, X. (2016). EERI Earthquake Reconnaissance Team Report: M7. 8 Muisne, Ecuador Earthquake on April 16, 2016.

Lee, W. H. K., & Lahr, J. C. (1972). *HYPO71: A computer program for determining hypocenter, magnitude, and first motion pattern of local earthquakes* (No. 72-224). US Geological Survey,.

León-Ríos, S., Ruiz, S., Maksymowicz, A., Leyton, F., Fuenzalida, A., & Madariaga, R. (2016). Diversity of the 2014 Iquique's foreshocks and aftershocks: clues about the complex rupture process of a Mw 8.1 earthquake. *Journal of Seismology*, *20*(4), 1059-1073.

Litherland, M. (1994). The metamorphic belts of Ecuador. *British Geological Survey, overseas Memoir.*, *11*.

Lonsdale, P. (2005). Creation of the Cocos and Nazca plates by fission of the Farallon plate. *Tectonophysics*, *404*(3), 237-264.

Luzieux, L. D. A., Heller, F., Spikings, R., Vallejo, C. F., & Winkler, W. (2006). Origin and Cretaceous tectonic history of the coastal Ecuadorian forearc between 1 N and 3 S: Paleomagnetic, radiometric and fossil evidence. *Earth and Planetary Science Letters*, *249*(3-4), 400-414.

Marcaillou, B., Spence, G., Collot, J. Y., & Wang, K. (2006). Thermal regime from bottom simulating reflectors along the north Ecuador–south Colombia margin: Relation to margin segmentation and great subduction earthquakes. *Journal of Geophysical Research: Solid Earth*, *111*(B12).

Marcaillou, B., Collot, J. Y., Ribodetti, A., d'Acremont, E., Mahamat, A. A., & Alvarado, A. (2016). Seamount subduction at the North-Ecuadorian convergent margin: Effects on structures, inter-seismic coupling and seismogenesis. *Earth and Planetary Science Letters*, *433*, 146-158.

Meissnar, R. O., Flueh, E. R., Stibane, F., & Berg, E. (1976). Dynamics of the active plate boundary in southwest Colombia according to recent geophysical measurements. *Tectonophysics*, *35*(1-3), 115-136.

Meltzer, A., Beck, S., Ruiz, M., Hoskins, M., Soto-Cordero, L., Stachnik, J. C., … Mercerat, E. D. (2019). The 2016 Mw 7.8 Pedernales Earthquake, Ecuador: RAPID Response Deployment. *Seismological Research Letters*.

Mendoza, C., & Dewey, J. W. (1984). Seismicity associated with the great Colombia-Ecuador earthquakes of 1942, 1958, and 1979: Implications for barrier models of earthquake rupture. *Bulletin of the seismological society of America*, *74*(2), 577-593.

Michaud, F., Proust, J. N., Collot, J. Y., Lebrun, J. F., Witt, C., Ratzov, G., ... & Penafiel, L. (2015). Quaternary sedimentation and active faulting along the Ecuadorian shelf: preliminary results of the ATACAMES Cruise (2012). *Marine Geophysical Research*, *36*(1), 81-98.

Mothes, P. A., Nocquet, J. M., & Jarrín, P. (2013). Continuous GPS network operating throughout Ecuador. *Eos, Transactions American Geophysical Union*, *94*(26), 229-231.

Nocquet, J. M., Jarrin, P., Vallée, M., Mothes, P. A., Grandin, R., Rolandone, F., ... & Régnier, M. (2017). Supercycle at the Ecuadorian subduction zone revealed after the 2016 Pedernales earthquake. *Nature Geoscience*, *10*(2), 145.

Pasten-Araya, F., Salazar, P., Ruiz, S., Rivera, E., Potin, B., Maksymowicz, A., et al (2018). Fluids along the plate interface influencing the frictional regime of the Chilean Subduction zone, northern Chile. *Geophysical Research Letters*, 45. https://doi.org/10.1029/2018GL079283

Peacock, S. M. (2001). Are the lower planes of double seismic zones caused by serpentine dehydration in subducting oceanic mantle?. *Geology*, *29*(4), 299-302.

Perfettini, H., Avouac, J. P., Tavera, H., Kositsky, A., Nocquet, J. M., Bondoux, F., ... & Soler, P. (2010). Seismic and aseismic slip on the Central Peru megathrust. *Nature*, *465*(7294), 78.

Pilger, R. H. (1984). Cenozoic plate kinematics, subduction and magmatism: South American Andes. *Journal of the Geological Society*, *141*(5), 793-802.

Reyes, P., & Michaud, F. (2012). Mapa Geologico de la Margen Costera Ecuatoriana (1500000) EPPetroEcuador-IRD. *Quito Ecuador*.

Rietbrock, A., Ryder, I., Hayes, G., Haberland, C., Comte, D., Roecker, S., & Lyon-Caen, H. (2012). Aftershock seismicity of the 2010 Maule Mw= 8.8, Chile, earthquake: Correlation between co-seismic slip models and aftershock distribution?. *Geophysical Research Letters*, *39*(8).

882 Rolandone, F., Nocquet, J. M., Mothes, P. A., Jarrin, P., Vallée, M., Cubas, N., ... & Font, Y.
883 (2018). Areas prone to slow slip events impede earthquake rupture propagation and
884 promote afterslip. *Science advances*, *4*(1), eaao6596.

885 Rothé, J. P. (1969). *The Seismicity of the Earty, 1953-1965: La Séismicité Du Globe 1953,*
886 *1965*. Unesco.

887 Ruiz, S., Klein, E., del Campo, F., Rivera, E., Poli, P., Metois, M., ... & Madariaga, R. (2016).
888 The seismic sequence of the 16 September 2015 M w 8.3 Illapel, Chile, earthquake.
889 *Seismological Research Letters*, *87*(4), 789-799.

890 Ruiz, S., Metois, M., Fuenzalida, A., Ruiz, J., Leyton, F., Grandin, R., ... & Campos, J. (2014).
891 Intense foreshocks and a slow slip event preceded the 2014 Iquique Mw 8.1 earthquake.
892 *Science*, *345*(6201), 1165-1169.

893 Ryder, I., Rietbrock, A., Kelson, K., Bürgmann, R., Floyd, M., Socquet, A., ... & Carrizo, D.
894 (2012). Large extensional aftershocks in the continental forearc triggered by the 2010 Maule
895 earthquake, Chile. *Geophysical Journal International*, *188*(3), 879-890.

896 Sallarès, V., & Charvis, P. (2003). Crustal thickness constraints on the geodynamic evolution
897 of the Galapagos Volcanic Province. *Earth and Planetary Science Letters*, *214*(3-4), 545-559.

898 Sallarès, V., Charvis, P., Flueh, E. R., Bialas, J., & SALIERI Scientific Party. (2005). Seismic
899 structure of the Carnegie ridge and the nature of the Galapagos hotspot. *Geophysical*
900 *Journal International*, *161*(3), 763-788.

901 Segovia, M. (2001). El sismo de Bahía del 4 de agosto de 1998: Caracterización del
902 mecanismo de ruptura y análisis de la sismicidad en la zonacostera. *Titulo de Ingeniera*
903 *Geologia (tesis): Escuela Politecnica Nacional, Quito, Ecuador*.

904 Segovia, M., Alvarado, A., Collot, J. Y., Sallares, V., & Pazmiño, N. (2009). Breve análisis de la
905 sismicidad y del campo de esfuerzos en el Ecuador. *Geología y Geofísica Marina y Terrestre*
906 *del Ecuador: desde la costa continental hasta las Islas Galápagos*, 131-149.

907 Segovia, M., Font, Y., Regnier, M. M., Charvis, P., Nocquet, J. M., Galve, A., ... & Ruiz, M. C.
908 (2015, December). Intense microseismicity associated with a SSE at La Plata Island in the
909 central subduction zone of Ecuador. In *AGU Fall Meeting Abstracts*.

910 Sennson, J. L., & Beck, S. L. (1996). Historical 1942 Ecuador and 1942 Peru subduction
911 earthquakes and earthquake cycles along Colombia-Ecuador and Peru subduction segments.
912 *Pure and applied geophysics*, *146*(1), 67-101.

913 Sokos, E. N., & Zahradnik, J. (2008). ISOLA a Fortran code and a Matlab GUI to perform
914 multiple-point source inversion of seismic data. *Computers & Geosciences*, *34*(8), 967-977.

915 Sokos, E., & Zahradník, J. (2013). Evaluating centroid-moment-tensor uncertainty in the new
916 version of ISOLA software. *Seismological Research Letters*, *84*(4), 656-665.

917 Storchak, D.A., D. Di Giacomo, I. Bondár, E. R. Engdahl, J. Harris, W.H.K. Lee, A. Villaseñor
918 and P. Bormann, 2013. Public Release of the ISC-GEM Global Instrumental Earthquake
919 Catalogue (1900-2009). Seism. Res. Lett., 84, 5, 810-815, doi: 10.1785/0220130034.

920 Toda, S., & Tsutsumi, H. (2013). Simultaneous reactivation of two, subparallel, inland normal
921 faults during the M w 6.6 11 April 2011 Iwaki earthquake triggered by the M w 9.0
922 Tohoku-Oki, Japan, earthquake. *Bulletin of the Seismological Society of America*, *103*(2B),
923 1584-1602.

924 Vaca, S., Régnier, M., Bethoux, N., Alvarez, V., & Pontoise, B. (2009). Sismicidad de la región
925 de Manta: Enjambre sísmico de Manta-2005. *Geologia y Geofisica Marina y Terrestre del*
926 *Ecuador Desde la Costa Continental Hasta las Islas Gapapagos*, 151-166.

927 Vaca, S. (2017). Interaction between tectonics, slow-slip processes and earthquake
928 mechanisms across the North Andean sliver (Ecuador). Thèse de doctorat de Sciences de la
929 Terre et de l'environnement. INSTITUT DE PHYSIQUE DU GLOBE DE PARIS.

930 Vaca, S., Vallée, M., Nocquet, J. M., Battaglia, J., & Régnier, M. (2018). Recurrent slow slip
931 events as a barrier to the northward rupture propagation of the 2016 Pedernales
932 earthquake (Central Ecuador). *Tectonophysics*, *724*, 80-92.

933 Vallée, M., Nocquet, J. M., Battaglia, J., Font, Y., Segovia, M., Regnier, M., ... & Yepes, H.
934 (2013). Intense interface seismicity triggered by a shallow slow slip event in the Central
935 Ecuador subduction zone. *Journal of Geophysical Research: Solid Earth*, *118*(6), 2965-2981.

936 Wadati, K., & Oki, S. (1933). On the travel time of earthquake waves.(Part II). *Journal of the*
937 *Meteorological Society of Japan. Ser. II*, *11*(1), 14-28.

938 White, S. M., Trenkamp, R., & Kellogg, J. N. (2003). Recent crustal deformation and the
939 earthquake cycle along the Ecuador–Colombia subduction zone. *Earth and Planetary Science*
940 *Letters*, *216*(3), 231-242.

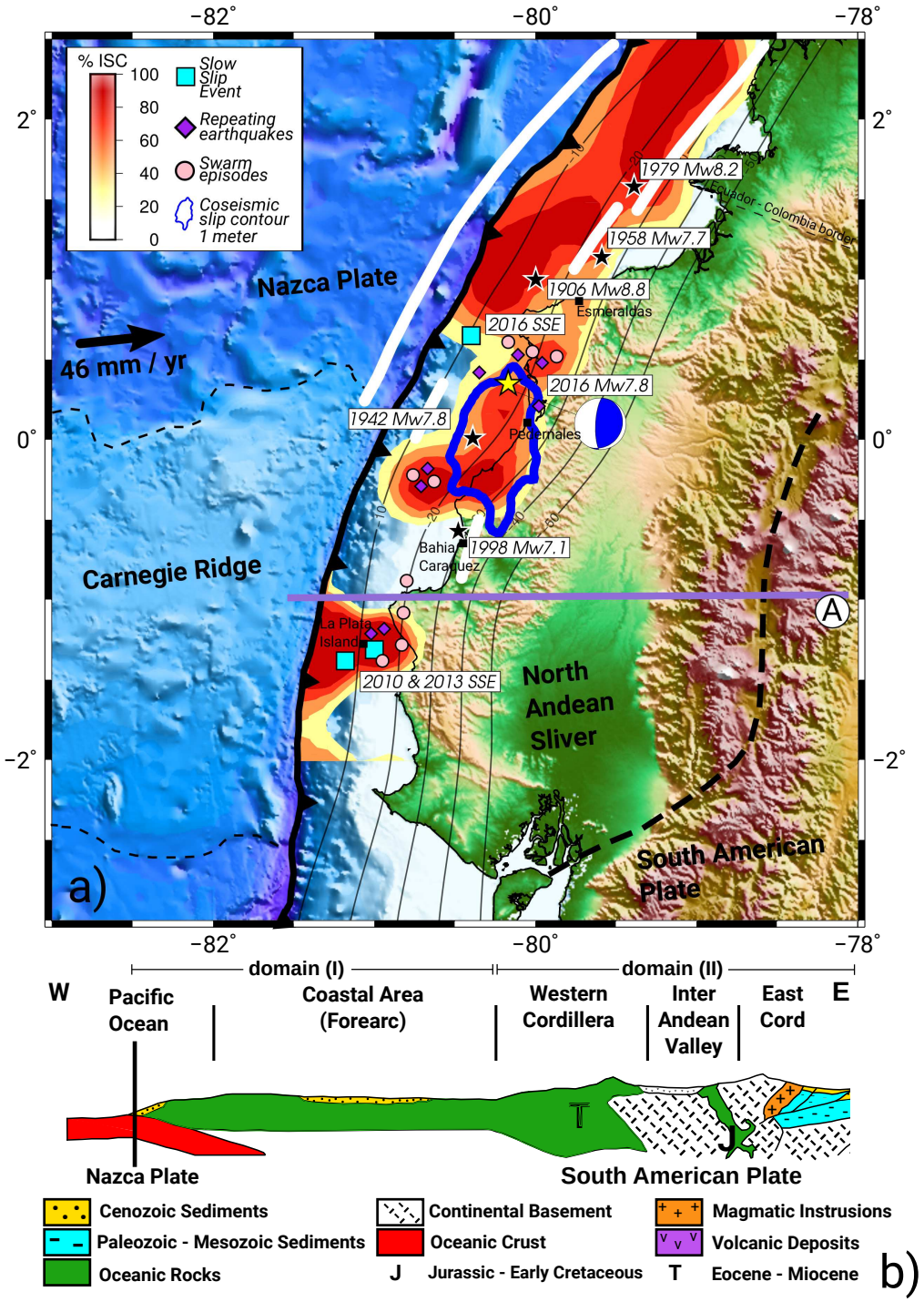

Figure 1: (a) Seismotectonic characteristics of the central coastal segment of the Ecuadorian margin. Inland and seafloor topography was derived by by Michaud et al. (2006). Segmented line shows the Dolores-Guayaquil Megashear that creates the North Andean Sliver. Bold arrow show the convergence rate between the Nazca plate and the North Andean Sliver (ref). Black stars and white solid lines represents the epicenters and estimated ruptures of the last large subduction earthquakes occurred along the margin since 1906. Squares, diamonds and circles are showing the Slow Slip Events, repeating earthquakes and swarms sequence, respectively, reported by Rolandone et al. (2018). Interseismic coupling derived by Nocquet et al. (2016) and Rolandone et al. (2018) is showed in background. Yellow star is showing the epicenter of the 2016 Mw 7.8 Pedernales earthquake. Focal mechanism and coseismic slip contour, in blue solid line, were obtained by Nocquet et al. (2016). Trench data from Collot et al. (2006). Purple solid line shows the location of the profile in Figure 1b. (b) Structural sketch of the Ecuadorian margin showing the main morphological structures. Figure edited from Janiard et al. (2000).

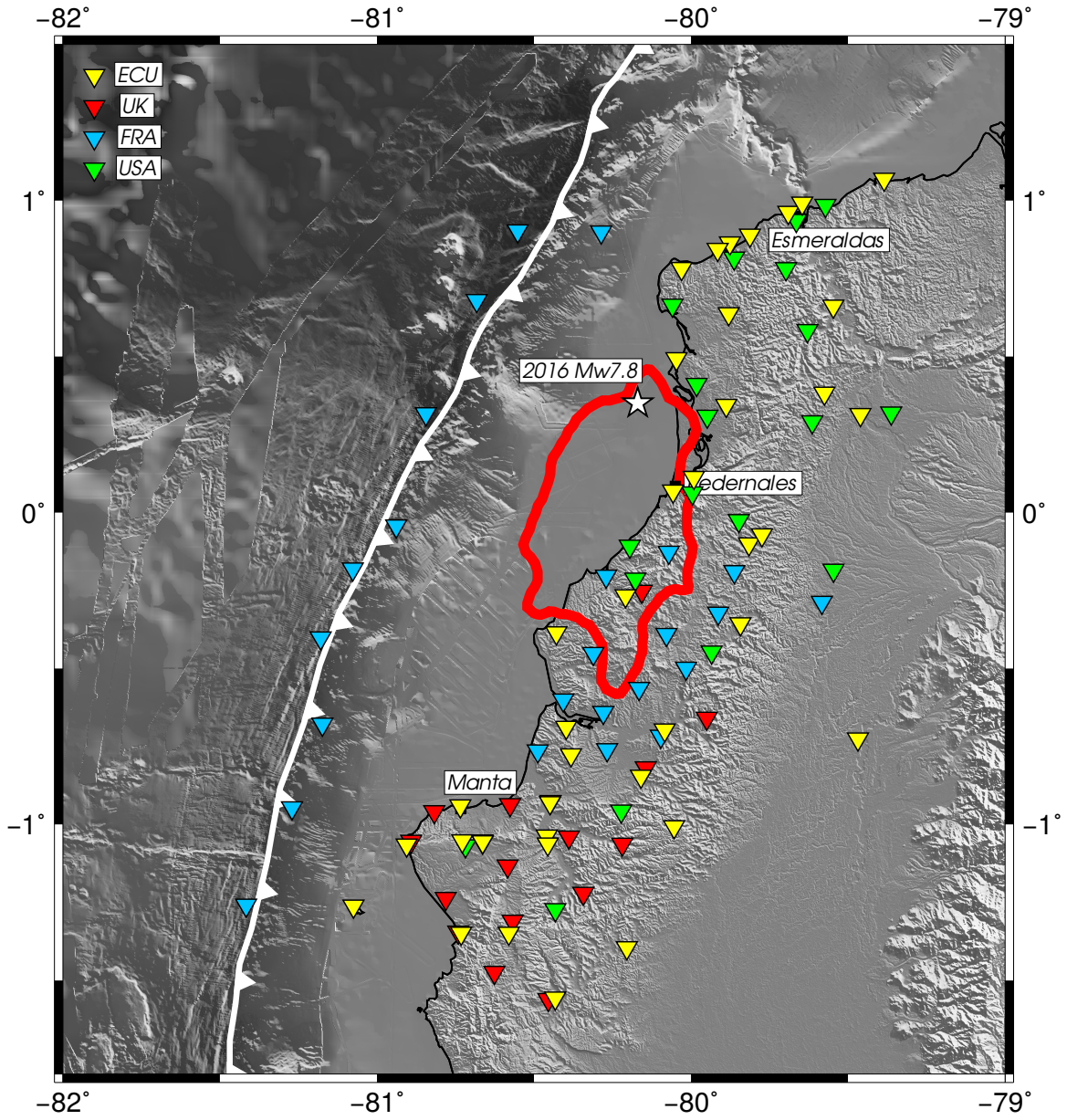

Figure 2: Seismic aftershock deployment. Inverted triangles represent the stations installed along the Ecuadorian margin. Yellow: backbone network including CMG-3ESP, Trillium compact, Trillium 120p, L4C, TSM-1 Strong Motion operated by the Instituto Geofisico de la Escuela Politecnica Nacional de Ecuador (IGEPN). Red: Broadband Trillium compact and short period Lennartz LE3D Lite instrumentation from the University of Liverpool, United Kingdom. Blue: intermediate period CMG-40T and Ocean Bottom Seismometers from GeoAzur, France. Green: Broadband Guralp CMG-3T and STS-2 from IRIS PASSCAL deployed by the University of Arizona and Lehigh University, United States. Most of the instruments deployed on site were recording at 100 Hz. White star is showing the epicenter of the 2016 Mw 7.8 Pedernales earthquake. Coseismic slip contour in red solid line was derived by Nocquet et al. (2016). Inland and seafloor topography was derived by Michaud et al. (2006). Trench data obtained from Collot et al. (2006).

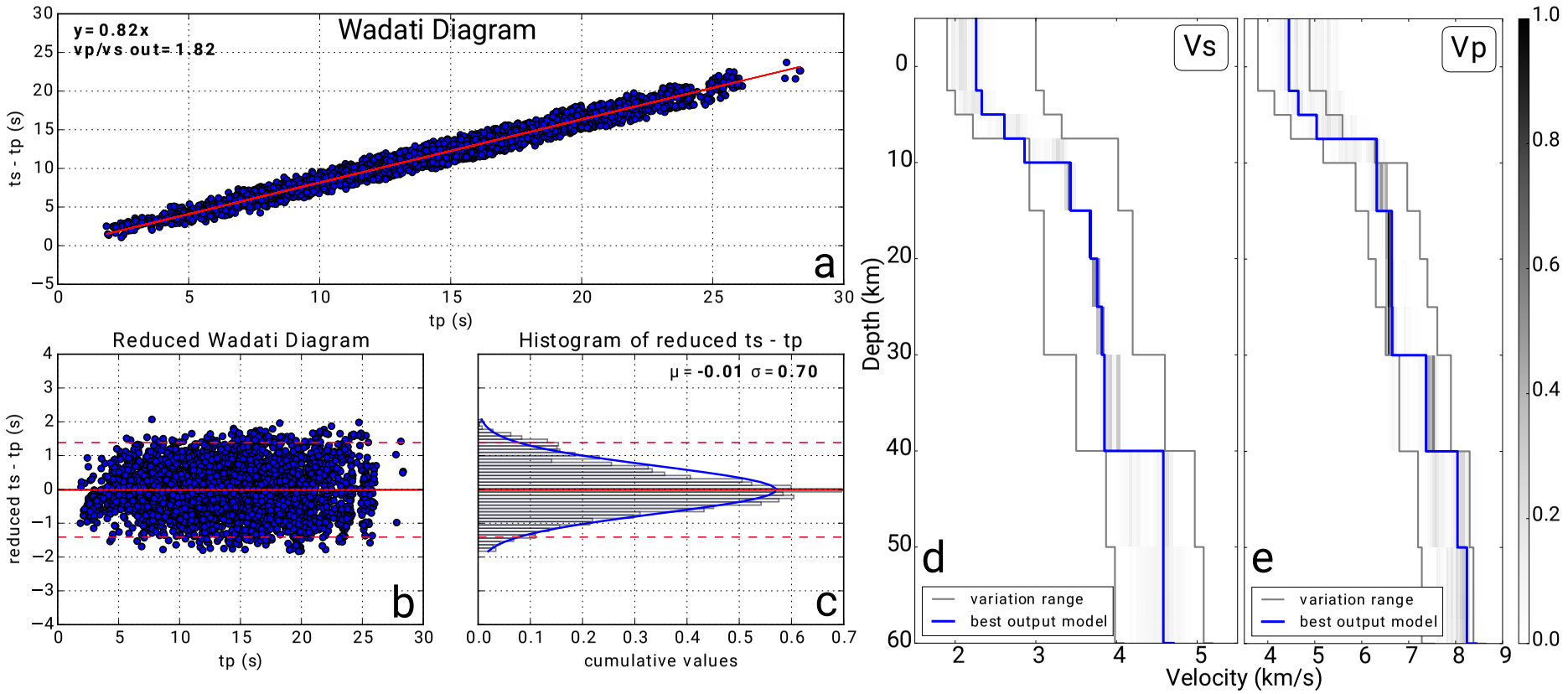

Figure 3: (a) Wadati Diagram (Wadati, 1933) used to compute the observed vp/vs ratio using all the available onsets. Red line shows the linear fit for the data which indicates a Vp/Vs ratio of 1.82. (b) Reduced Wadati Diagram used to remove outliers from onset times picked. $|Vp/Vs| > 2\sigma$ was used as a cutoff value. Solid red line: $y = 0$. Segmented red line: $y = \pm 2\sigma$. (c) Reduced ts - tp histogram showing the distribution of picks in terms of its reduced time. Solid red line: $y = 0$. Segmented red line: $y = \pm 2\sigma$. (d) and (e) Density plot for S-wave and P-wave velocity model, respectively, showing the best 200 solutions. Solid blue line shows the solution with the lowest rms. Gray lines are the perturbation range for each phase. Colorbar indicates the normalized hit count on each output model.

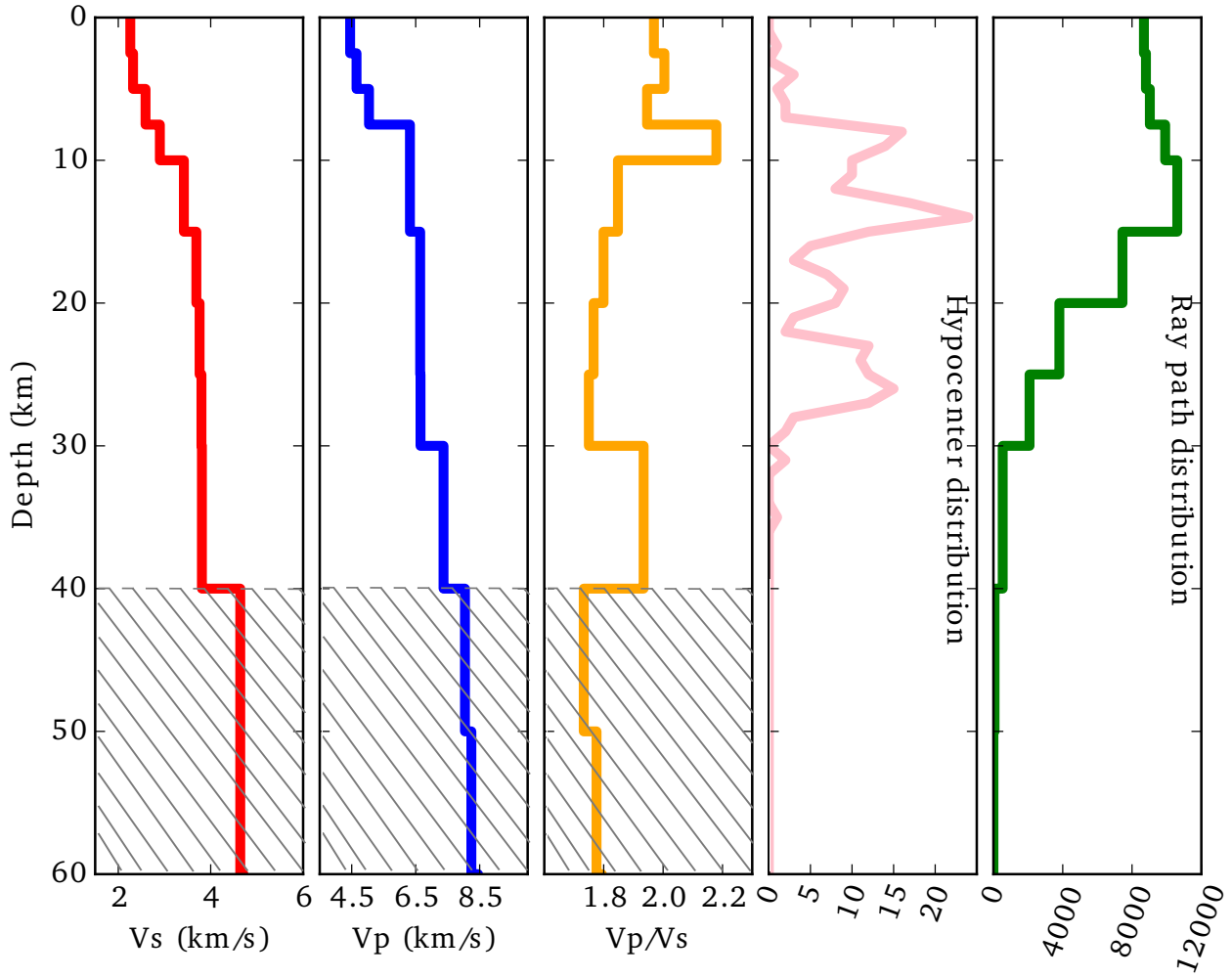

Figure 4: Final 1D velocity model showing the absolute Vp (solid blue line) and Vs (solid red line) velocities, Vp/Vs ratio (solid orange line) and a histogram of the seismicity distribution with depth. Dashed area indicates the area where our minimum 1D model is unconstrained. Velocity values for depths greater than 40 km were derived by Font et al. (2013) and were included in our initial reference model.

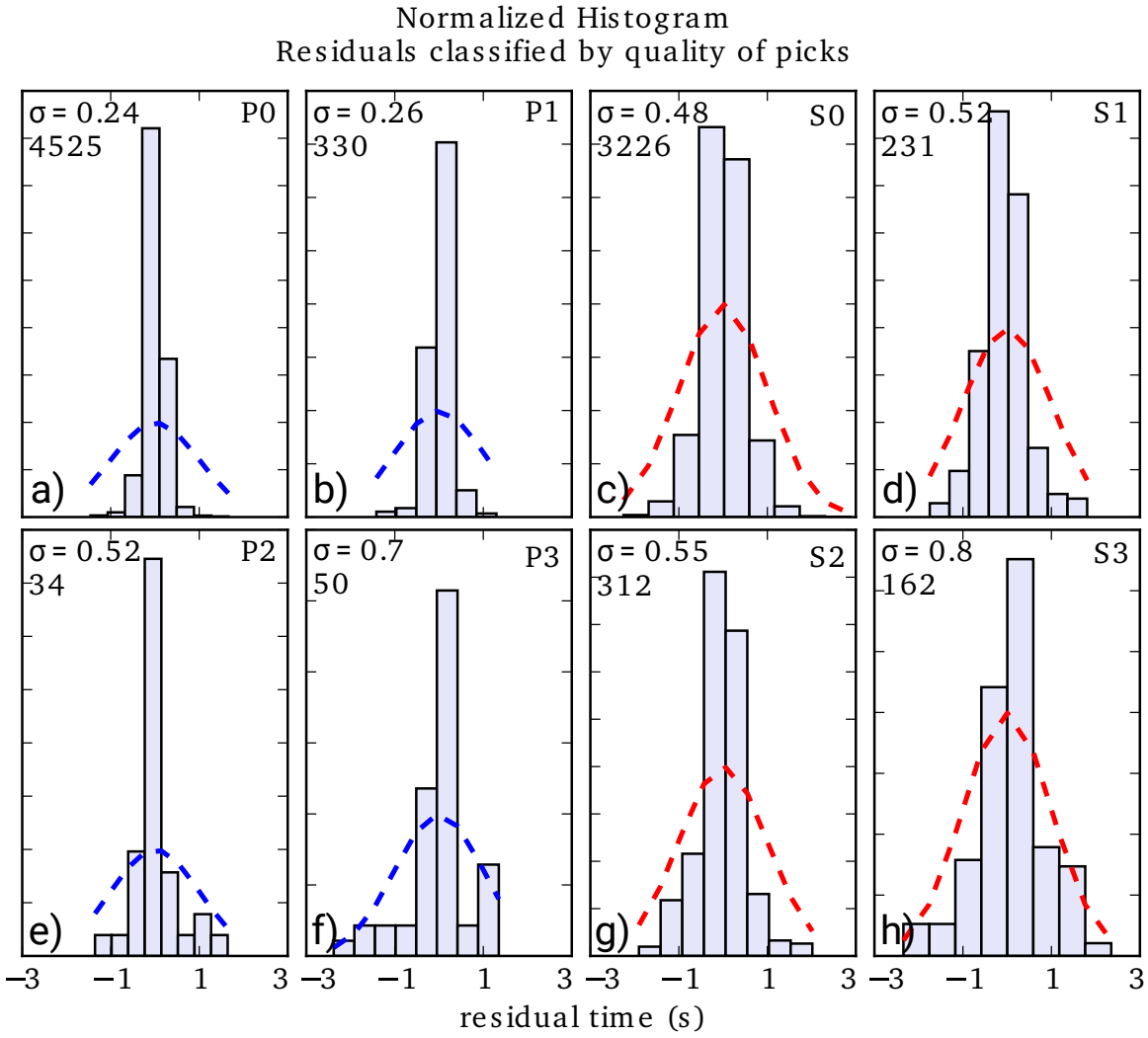

Figure 5: Histograms for the residuals obtained after the inversion of both Vp and Vs velocities. Plots were classified according to the quality of picks indicated in the top right corner. Each weight corresponds to the following time uncertainties: Weight 0 ($<$ 0.04 s); Weight 1 (0.04 – 0.1 s); Weight 2 (0.1 – 0.2 s); Weight 3 (0.2 – 1 s); Weight 4 ($>$ 1 s). Segmented blue and red lines represent the fit of the data. Standard deviation and number of observation are displayed on the top left corner of each plot.

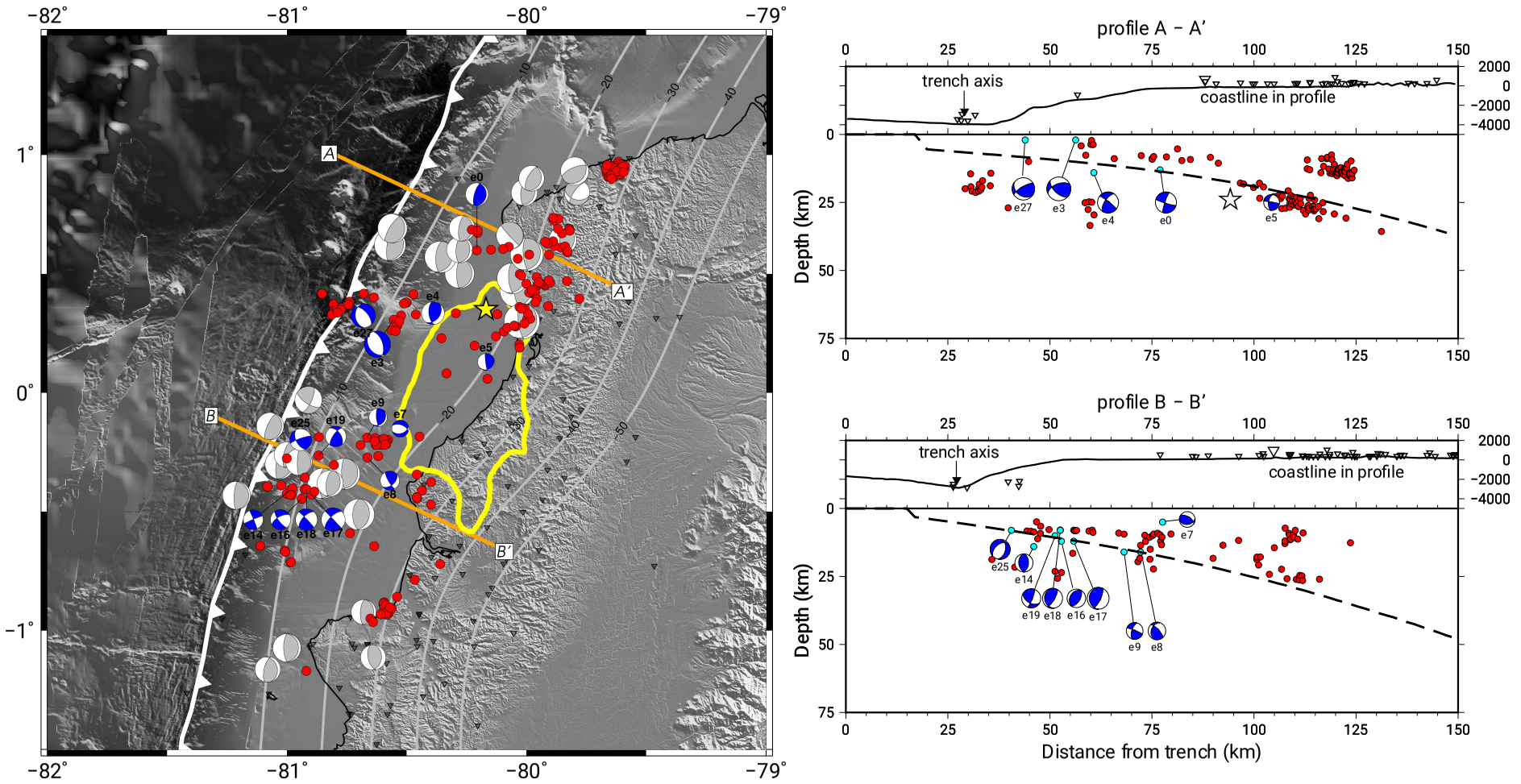

Figure 6: Mapview and cross sections, 60 km wide, of the relocated seismicity. Red circles indicate the aftershock locations after the inversion with VELEST. Blue beach balls represent the RMT calculated using isola superimposed over the gCMT catalog in gray. Star shows the location of the 2016 Mw 7.8 Pedernales earthquake. Slab1 from Hayes et al. (2012) is being used as a reference for the in-depth distribution. Inland and seafloor topography from Michaud et al. (2006). Coseismic slip contour derived by Nocquet et al. (2016). Inland and seafloor topography from Michaud et al. (2006). Trench data obtained from Collot et al. (2006). Slab 1.0 km depth contours from Hayes et al. (2012) are shown in gray lines.

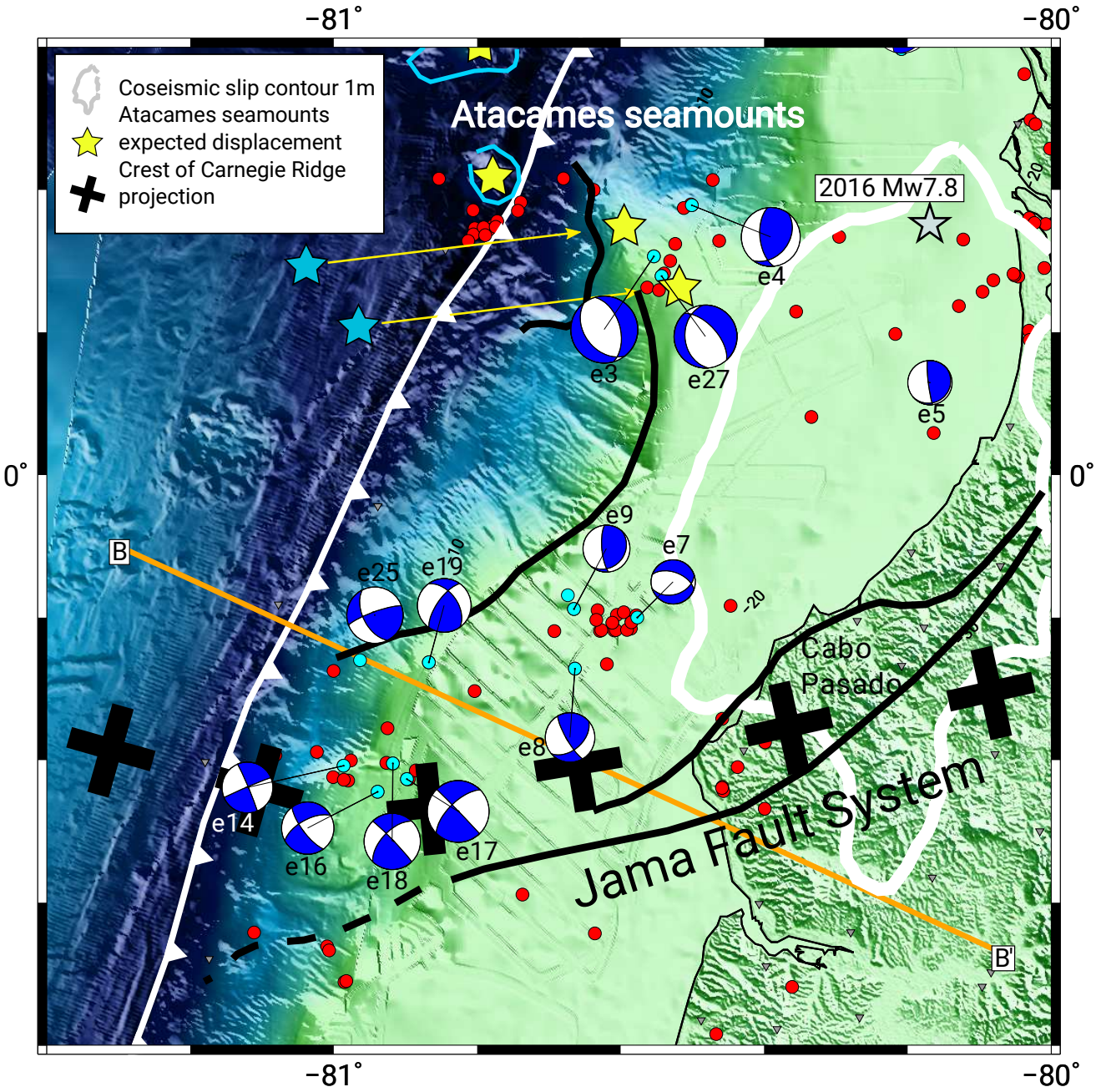

Figure 7: Zoom into the offshore Cabo Pasado area, where the strike-slip seismicity was detected. Red circles represents the seismicity relocated in the 1D inversion. Blue beach balls are the RMT solutions. Black crosses are the projection of the crest of the CR derived by Collot et al. (2004). Black solid lines show the Jama Fault System and its projection off shore from Collot et al. (2004) and Reyes Michaud (2012), and the scarps in the marine forearc. Blue and yellow stars are the initial and final position of the Atacames seamounts proposed by Marcaillou et al. (2016). Grey star shows the epicenter of the 2016 Mw 7.8 Pedernales earthquake. Coseismic slip contour derived by Nocquet et al. (2016) is indicated in solid yellow line. Inland and seafloor topography from Michaud et al. (2006). Trench data obtained from Collot et al. (2006). Slab 1.0 km depth contours from Hayes et al. (2012) are shown in gray lines.

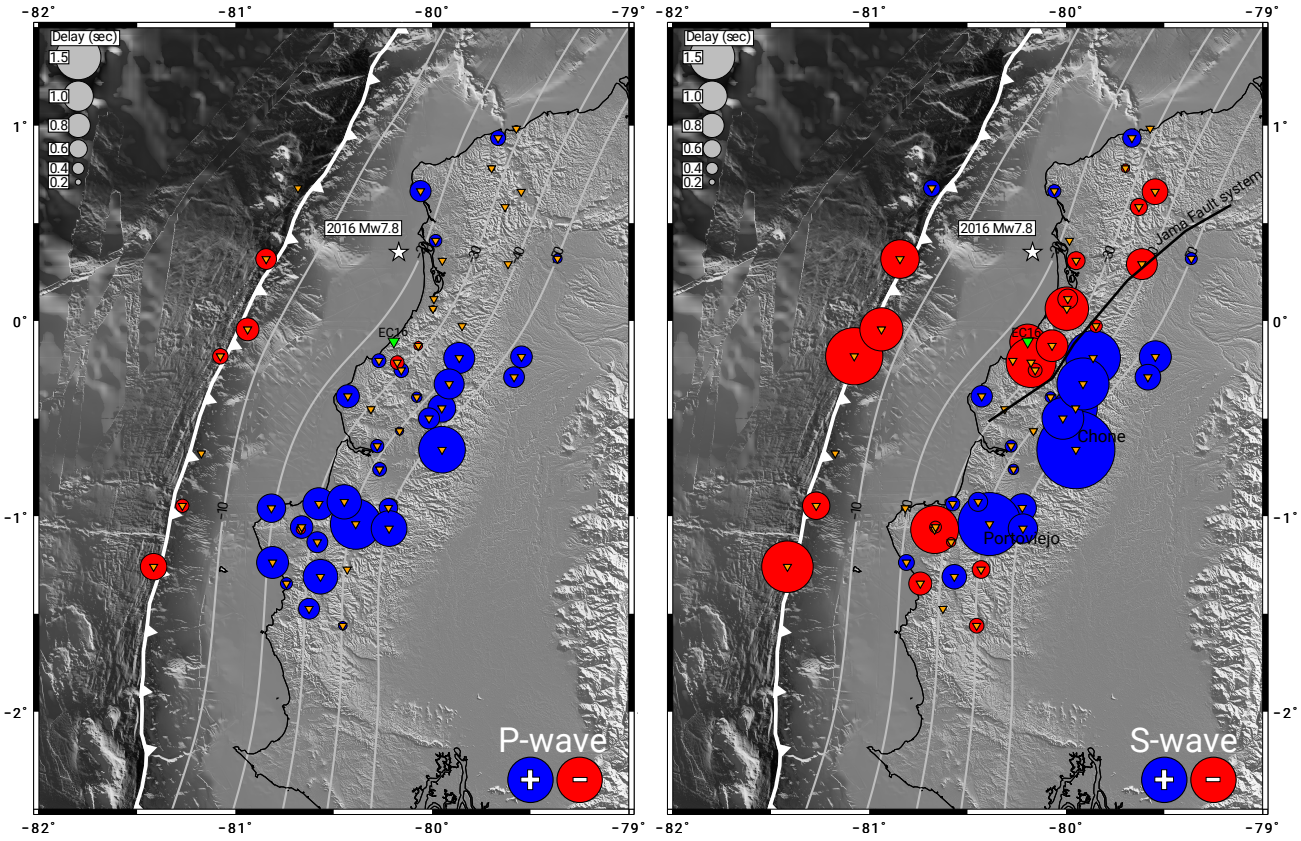

Figure 8: Map with station corrections for P- (right) and S- (left) phases obtained after the 1D inversion. Inverted green triangle represents the reference station EC16. White star is showing the epicenter of the 2016 Mw 7.8 Pedernales earthquake. Inland and seafloor topography from Michaud et al. (2006). Trench data obtained from Collot et al. (2006). Slab 10 km depth contours from Hayes et al. (2012) are shown in gray lines. Jama Fault System (JFS) trace extracted from Reyes Michaud (2012).